Geophysical Journal International

Geophys. J. Int. (2021) **227,** 1665–1681
Advance Access publication 2021 July 19
GJI Seismology

https://doi.org/10.1093/gji/ggab278

Seismic anisotropy, dominant slip systems and phase transitions in the lowermost mantle

Brian Chase Chandler,[1] Li-Wei Chen,[1] Mingming Li,[2] Barbara Romanowicz[1,3,4] and Hans-Rudolf Wenk[1]

[1] *Department of Earth and Planetary Science, U.C. Berkeley, Berkeley, CA* 94720, *USA. E-mail: wenk@berkeley.edu*
[2] *School of Earth and Space Exploration, Arizona State University, Tempe, AZ* 85287, *USA*
[3] *Collège de France,* 75231 *Paris, France*
[4] *Institut de Physique du Globe, Université de Paris,* 75005 *Paris, France*

Accepted 2021 July 9. Received 2021 July 8; in original form 2021 January 8

SUMMARY

The presence of seismic anisotropy at the base of the Earth's mantle is well established, but there is no consensus on the deformation mechanisms in lower mantle minerals that could explain it. Strong anisotropy in magnesium post-perovskite (pPv) has been invoked, but different studies disagree on the dominant slip systems at play. Here, we aim to further constrain this by implementing the most recent results from atomistic models and high-pressure deformation experiments, coupled with a realistic composition and a 3-D geodynamic model, to compare the resulting deformation-induced anisotropy with seismic observations of the lowermost mantle. We account for forward and reverse phase transitions from bridgmanite (Pv) to pPv. We find that pPv with either dominant (001) or (010) slip can both explain the seismically observed anisotropy in colder regions where downwellings turn to horizontal flow, but only a model with dominant (001) slip matches seismic observations at the root of hotter large-scale upwellings. Allowing for partial melt does not change these conclusions, while it significantly increases the strength of anisotropy and reduces shear and compressional velocities at the base of upwellings.

Key words: Phase transitions; Plasticity, diffusion, and creep; Mantle processes; Seismic anisotropy; Rheology: mantle.

1 INTRODUCTION

The deepest 200–300 km of the Earth's mantle form a complex thermal and mechanical boundary layer, D" (Bullen 1949), where the dynamics remain surprisingly elusive. Our current understanding of D" is guided by seismological observations which indicate the presence of significant laterally varying shear wave anisotropy in this region, in contrast to the bulk of the lower mantle which is largely isotropic (see review by Romanowicz & Wenk 2017). Indeed, it has been proposed that large strains during flow in the deep mantle could lead to crystal preferred orientation (CPO) of anisotropic minerals (also referred to as texture) such as the high-pressure magnesium post-perovskite (pPv), which could explain the seismic anisotropy observations (e.g. McNamara *et al.* 2002, 2003; Wenk *et al.* 2011).

Most seismological studies of D" anisotropy rely on splitting measurements of shear waves diffracted (Sdiff) or reflected (ScS) on the core–mantle boundary (CMB, Nowacki *et al.* 2011), as well as core phases SKS/SKKS (Long 2009; Nowacki *et al.* 2011). While such data sample the D" locally, the limited available earthquake source and receiver locations restrict azimuthal coverage. Their interpretation thus relies on simplified models of anisotropy, mainly vertically transverse isotropy (VTI, also referred to as radial anisotropy), in which the speeds of horizontally and vertically polarized waves are different (V_{SH} and V_{SV}, respectively). In general, $V_{SH} > V_{SV}$ is found in regions of faster than average isotropic shear wave velocity (V_{Siso}), as imaged by seismic tomography, and attributed to the 'graveyard' of cold slabs. In contrast, $V_{SH} < V_{SV}$ or no significant splitting is found in regions of slower than average V_{Siso} such as the large low shear velocity provinces (LLSVPs) beneath the central Pacific and Africa (e.g. Cottaar & Romanowicz 2013; Lynner & Long 2014, Fig. 1). There have also been some attempts at resolving a tilted fast axis of anisotropy (TTI, e.g. Garnero *et al.* 2004; Pisconti *et al.* 2019).

While CPO could explain the observed anisotropy, consensus has yet to be reached on the underlying deformation mechanisms that could give rise to the observed bulk anisotropic signatures (Cottaar *et al.* 2014; Walker *et al.* 2018; Tommasi *et al.* 2018). Some studies propose that (010) is the preferred slip plane in pPv, as found from theoretical computations (Goryaeva *et al.* 2016; 2017), while

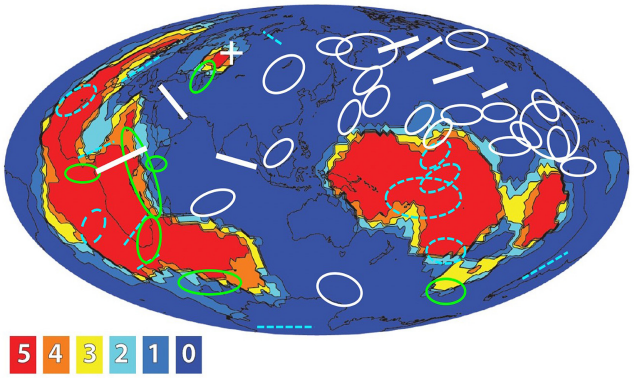

Figure 1. Observations of radial anisotropy in D". Background: 'Voting map' based on five shear wave velocity tomographic models showing the locations in D" where the five models agree that *Vs* is lower than average (red) or higher than average (dark blue), highlighting the location of the two LLSVPs and the ring of fast velocities around them. Superimposed ellipses and lines indicate regions where shear wave splitting measurements have inferred $V_{SH}>V_{SV}$ (white), $V_{SH}<V_{SV}$ (magenta dashed) or the presence of strong lateral variations in anisotropy (green). The latter is found at the borders of the LLSVP and near the PERM anomaly indicated by a white cross. Modified after Romanowicz & Wenk (2017).

others favour a (001) slip plane (Nowacki *et al.* 2011; Cottaar *et al.* 2014), in agreement with experimental results (Miyagi *et al.* 2010; Wu *et al.* 2017) or anisotropic diffusion creep leading to crystal alignment (Dobson *et al.* 2019). Dominant slip on (100) has also been proposed (Merkel *et al.* 2007; Walker *et al.* 2011) but has been shown to provide a poor match to the observed seismic signatures (Wenk *et al.* 2011; Cottaar *et al.* 2014) so we have chosen not to include it in this investigation.

Because an anisotropic signature is unique to a specific mineral (or combination of minerals) under specific pressure (P) and temperature (T) conditions as well as deformation geometries, all of which vary from region to region, a model that explores spatially varying environments is needed to better understand the possible causes of lowermost mantle anisotropy observations. This need arises due to the various flow regimes present in the lower mantle. For instance, certain parameters or configurations may explain the observed anisotropic signature in regions of downwelling flow, but not in regions of horizontal flow experienced during CMB traversal or in plume-like upwellings, or some other combination of the above. By exploring these flow regimes as they transition from one to the other, a fuller picture can begin to take shape.

Here, we build upon previous multidisciplinary work, in which we considered a 3D geodynamic model of a subducting slab driven by solid state convection as it penetrates into the lower mantle and impinges on the CMB (Cottaar *et al.* 2014). Combining the strain inferred from the flow field with a polycrystal plasticity model (Lebensohn & Tomé 1993) and knowledge from mineral physics on the elasticity of pure orthorhombic $MgSiO_3$ endmember phases of bridgmanite (Pv) and post-perovskite (pPv, Zhang *et al.* 2016), as well as cubic periclase (MgO, Karki *et al.* 2000) and Ca-perovskite ($CaSiO_3$, CaPv, Kawai & Tsuchiya 2015), we calculated the resulting seismic anisotropy, including spatial and depth variations, due to deformation by dislocation glide within a slab with pyrolitic composition and compared them with seismic observations.

The present study differs from the previous one (Cottaar *et al.* 2014) in four important aspects: (1) we use a realistic combination of 3 minerals thought to be the dominant phases in the lower mantle in proportions consistent with a pyrolite composition; (2) we introduce a layer of intrinsically denser-than-average material at the base of the mantle, which is pushed around by the descending slab into thick thermochemical piles, from which upwellings initiate, which allows us to examine the character of the resulting seismic anisotropy and isotropic velocities ($V_{\rm Siso}$), not only in the downwelling part of the slab but also in the region of onset of upwelling; (3) assuming pressure (P) as inferred from the Preliminary Reference Earth Model (PREM, Dziewonski & Anderson 1981) and considering temperature (T) variations throughout the geodynamic model, we take into account forward (Pv to pPv) and reverse (pPv to Pv) phase transitions in the lowermost mantle and the associated texture inheritance that may occur; and lastly 4) we introduce partial melting in the deepest portions of the slab at the base of upwelling. We then compare two scenarios, which differ by the choice of dominant slip systems for pPv, (001) slip for Model 001 (Miyagi *et al.* 2010; Wu *et al.* 2017), and (010) slip for Model 010 (Goryaeva *et al.* 2016, 2017; Tommasi *et al.* 2018). We extract maps of radial anisotropy described by the parameter $\xi = (Vsh/Vsv)^2$ and also compute shear wave splitting (SWS) directions and strength of splitting (as $100 \cdot \frac{2(V_{S1}-V_{S2})}{V_{S1}+V_{S2}}$) of a seismic wave that propagates horizontally in D", such as Sdiff or ScS.

2 METHODS

2.1 3-D geodynamic model

Originally 2-D geodynamic models were applied to predict seismic anisotropy in the upper part of the lower mantle (Wenk *et al.* 2006) and the D" zone (Wenk *et al.* 2011). Here, we focus on 3-D simulations. As the 3-D geodynamic model (Cottaar *et al.* 2014; Li & Zhong 2017) provides the framework for the macroscopic deformation, it will be described first. The geodynamic model used here was developed using a modified version of CitcomCU under the standard Boussinesq approximation for solving the non-dimensional equations of mass, momentum, and energy (eqs 1–3, e.g. Zhong 2006) along the same lines as previous works (Cottaar *et al.* 2014).

$$\nabla \cdot \vec{u} = 0 \tag{1}$$

$$-\nabla P + \nabla \cdot (\eta \dot{\epsilon}) = Ra\,(T - BC)\hat{r} \tag{2}$$

$$\frac{\partial T}{\partial t} + (\vec{u} \cdot \nabla)\, T = \nabla^2 T + H, \tag{3}$$

where $\vec{u}$ is the velocity, P is the pressure, η is the viscosity, $\dot{\epsilon}$ is the strain rate, Ra is the Rayleigh number, T is the temperature, B is the buoyancy number, C is the composition, $\hat{r}$ is a unit vector in radial direction, t is the time and H is the internal heating rate. The Rayleigh number is defined as:

$$Ra = \frac{\rho g \alpha \Delta T R^3}{\kappa \eta_0}, \tag{4}$$

where ρ, g, α, κ and η_0 are, respectively, the reference density, gravitational acceleration, thermal expansivity, thermal diffusivity and reference viscosity. The ΔT is the reference temperature which equals to the temperature different between the surface and the CMB. R is the Earth's radius. In this study, we use $Ra = 5.36 \times 10^8$. The buoyancy number is defined as:

$$B = \frac{\Delta \rho}{\rho \alpha \Delta T}, \tag{5}$$

Table 1. Geodynamic parameters used in this study.

Parameters	Reference value
Earth's radius, R	6371 km
Mantle thickness	2890 km
Mantle density, ρ	3300 kg m^{-3}
Thermal expansivity, α	3×10^{-5} K^{-1}
Thermal diffusivity, κ	1×10^{-6} m^2 s^{-1}
Gravitational acceleration, g	9.8 m s^{-2}
Temperature change across the mantle, ΔT	3000 K
Reference viscosity, η_0	1.4×10^{21} Pa s

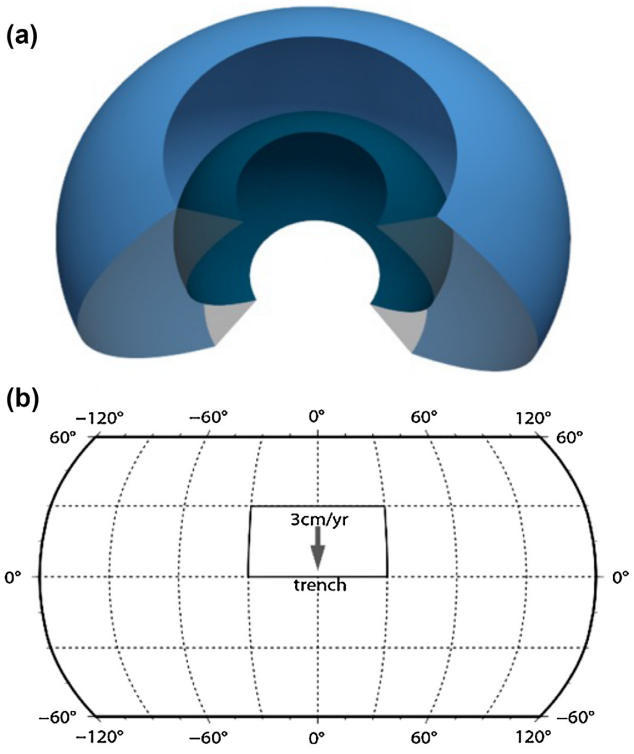

Figure 2. Setup of geodynamic model. (a), 3-D view of the model domain that covers a depth range of from the surface (blue) to the CMB (green), a longitude range of –120° to 120°, and a latitude range of –60° to 60°. (b), 2-D view of the top surface of the model domain. The subducting plate, which is outlined by the solid thick black lines, is imposed with a constant southward angular velocity of 3 cm yr^{-1}. The surface velocity is zero outside the subducting plate.

where $\Delta\rho$ is the density anomaly with respect to the background mantle. The physical parameters used in the geodynamic model are listed in Table 1.

The model domain has a longitude range of –120° to 120°, a latitude range of –60° to 60°, and a depth ranging from the surface to the CMB (Figs 2a and b). There are 128, 256 and 512 elements in the radial, latitudinal and longitudinal directions, respectively. All boundaries are free-slip except the surface which has a southward constant angular velocity of 3 cm yr^{-1} in the region bounded by latitude of 0–30° and longitude of –30° to 30° and zero velocity outside (Fig. 2b). The temperature is isothermal on both top ($T = 0$) and bottom ($T = 1$) and insulating on the sides. The model is also internally heated with $H = 60$.

The viscosity is both temperature- and depth-dependent and is defined as:

$$\eta = \eta(r)\exp\left[A\left(0.6 - T\right)\right], \tag{6}$$

where A is the dimensionless activation energy and we use $A = 9.21$, which corresponds to a dimensional activation energy of $\sim$190 kJ mol^{-1}. The $\eta(r)$ is the depth-dependent viscosity pre-factor as a function of the dimensionless radius r, and is given by:

$$\eta(r) = \begin{cases} 1.0, & r > 0.8964 \\ 30 \times (24.1 - 25.7r), & r \leq 0.8964 \end{cases}, \tag{7}$$

such that the $\eta(r)$ increases from 1.0 to 30.0 across the 660 km discontinuity, as suggested by (Hager 1984), and it continues to increase linearly by 10 times from 660 km to the CMB, similar to that in (Li & Zhong 2017).

Adding complexity to our previously presented models which focused only on slab impingement on the CMB (Cottaar *et al.* 2014), here, a global layer of intrinsically dense material is introduced initially at the bottom of the mantle, with a thickness of 300 km and a buoyancy number of $B = 0.8$ (i.e. $\Delta\rho/\rho = 2.4$ %). This dense material is later pushed by a subducted slab into thermochemical piles in the lowermost mantle (green structure in Figs 3a–c).

Passive Lagrangian tracers are allowed to subduct with slab material and record the velocity gradient (and therefore strain rate as shown in Figs 3d and e) at each time step which are then used to calculate the resultant deformation within the aggregate. The position, temperature, and velocity gradient at each time-step is then extracted and combined with the radial pressure provided by PREM, which is interpolated to each passive tracer within the model. A surface temperature of 273.5 K and an average adiabatic temperature gradient of 0.35 K km^{-1} are applied when converting non-dimensional temperatures to dimensional temperatures at passive Lagrangian tracers, and tracers at the CMB have a dimensional temperature of 4285 K. The path-lines of tracers used in this study were selected based on a spatial distribution to sample various deformation geometries present in the slab. Therefore, 25 individual path-lines were selected with multiple sampling from areas including (1) paths nearest to the CMB, (2) paths near the edge of the slab that may experience effects due to the spreading of the slab as it impacts the CMB, (3) areas within the bulk of the slab (away from edges) and (4) sections of the top layer of the slab that fail to meet the phase transition criteria depicted in Fig. 4(a). These path-lines all begin above 1000 km depth and end at various heights above the CMB in the upwelling area (radial depths of 1200–2000 km) and contain between 400 and 600 deformation steps. Note that this geodynamic model does not include any information about texture development which may alter the flow path. It treats the mantle as a homogeneous isotropic medium. We will address this issue later.

2.2 Plastic deformation within the slab

Here we assume a pyrolite composition of 3 phases (17 % periclase (MgO), 9 % $CaSiO_3$ (CaPv) and 74 % bridgmanite (Pv) which transforms to post-perovskite (pPv) in D"). The aggregate entered into each path-line is represented by an initial set of 1000 randomly oriented spherical grains which are plastically deformed according to the recorded velocity gradient along the slab's subduction using the viscoplastic self-consistent deformation code VPSC (Lebensohn & Tomé 1993). This approach allows us to simulate the plastic deformation of aggregate material by solving the constitutive equations under the Eshelby inclusion formalism in which an inclusion (here a grain) is imbedded in a fully anisotropic, yet homogenous, medium (Eshelby 1957). Each grain is subjected to external stresses and strains and the resulting deformation is caused by slip of dislocations on various slip systems. The strain rate $\dot{\varepsilon}$ is related to the applied stress σ according to the power law $\dot{\varepsilon} \propto \sigma^n$. Here we

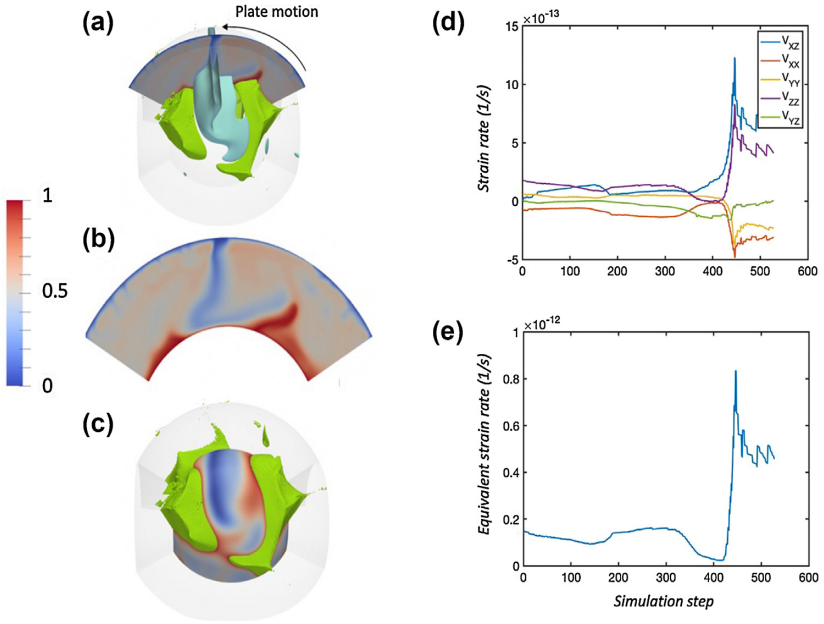

Figure 3. Geodynamic model showing (a) cold slab (blue) impinging on CMB pushing intrinsically dense materials into thermochemical pile (green). (b) Cross section showing non-dimensional temperature (scalebar) variations taken through the slice indicated in grey in (a). (c) Non-dimensional temperature variations at the base of the slab with slab removed. (d) Equivalent strain rates and (e) component strain rates for a select path-line at each deformation step are shown in depicting the varying strain regimes as the slab motion evolves.

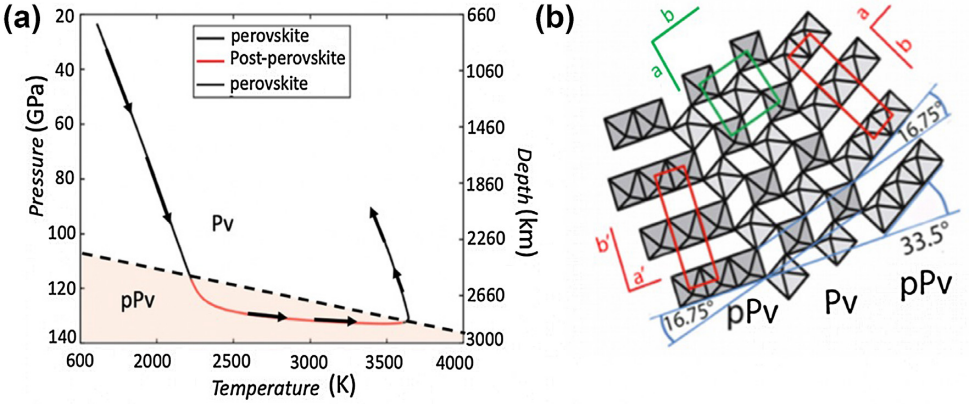

Figure 4. (a), Pressure (P)-temperature (T) phase diagram of Pv and pPv with a penetrating slab (arrows) experiencing varying conditions as a function of depth and position, transforming from Pv (black) to pPv (red) and back to Pv. Dashed line is Clapeyron slope (Oganov & Ono 2004), and orange shaded area shows P–T conditions where the pPv phase can exist in this model. (b), Topotaxial relationship for the Pv–pPv phase transition considered in this study with green representing the Pv unit cell and red the pPv unit cell (Dobson *et al.* 2013).

assume a stress exponent $n = 3$, corresponding to the dislocation creep regime. Although various deformation mechanisms have been proposed to take place in the lower mantle such as pure dislocation climb (Boioli *et al.* 2017) and diffusion (Ammann *et al.* 2010), these mechanisms, contrary to dislocation glide, are considered not to produce significant crystal rotations, and can act to weaken existing CPO. Contributions from such non-rotational mechanisms are incorporated here indirectly by assuming 50 % of the accrued strain to contribute to plastic deformation by dislocation glide as was done in our previous studies (Wenk *et al.* 2011; Cottaar *et al.* 2014). It has also been argued that diffusion creep may preserve CPO (Wheeler 2009) and furthermore that anisotropic diffusion can lead to the development of CPO (Dobson *et al.* 2019). Here, we concentrate only on the slab material itself where dislocation creep is expected to dominate (McNamara *et al.* 2003).

Plastic deformation occurs on a specific slip system when the applied stress exceeds the critical resolved shear stress (CRSS). Values used in this model for each assumed active system are shown for each phase in Table 2. In reality CRSS changes with deformation and temperature but we keep it constant for the whole deformation path. We use values of Amodeo *et al.* (2011) for pure end member MgO, of Mainprice *et al.* (2008) for Pv, of Miyagi *et al.* (2009) for $CaSiO_3$ and two variations of slip systems for the pPv phase. Model 001 contains systems based on high pressure experiments by Miyagi *et al.* (2011) while Model 010 is based on ab-initio calculations of Goryeva *et al.* (2016, 2017) also used by Tommasi *et al.* (2018). For all phases a lowest CRSS of 1 was assigned, even though there is some evidence that MgO may be weaker (e.g. Miyagi & Wenk 2016; Kasemer *et al.* 2020). We keep this at value at 1 to conform with Tommasi *et al.* (2018). Since MgO and CaPv

Table 2. Deformation mechanisms (slip systems) and relative CRSS values used for each model in this study. Relative CRSS values are provided for each system. (a) Mainprice *et al.* (2008), (b) Amodeo *et al.* (2011), (c) Miyagi *et al.* (2009), (d) Miyagi *et al.* (2011), (e) Goryaeva *et al.* (2016, 2017). Slip system activity (per cent) which represents the sum of relative amounts of shear contributed by each phase is given at two locations along a selected path-line at 200 steps after initiation and then 100 steps after the Pv–pPv transition.

Phase %	Slip system	CRSS	Act. % Step 200	Act % 100 steps after transition	Phase %	Slip System	CRSS	Act. % Step 200	Act % 100 steps after transition**
Pv[a] 74 %	(010)[100]	1.8	2.6	*	MgO[b]**	$\{1\bar{1}0\}<110>$	1	14.4	16.4
	(001)[100]	2.5	5.6	*	17 %	{100}<110>	1	10.2	10.9
	(100)[010]	1	15.4	*		{111}<110>	g	4.7	5.2
	(001)[010]	1	2.6	*				**29.3**	**32.5**
	(100)[001]	3.8	1.6	*					
	(010)[001]	1.6	5.1	*	CaPv[c]**	$\{1\bar{1}0\}<110>$	1	5.7	6.4
	$\{\bar{1}10\}$[001]	1.9	7.6	*	9 %	{100}<110>	1.5	4.5	5.4
	$(001)<\bar{1}10>$	1.8	8.1	*		{111}<110>	3.0	0.7	0.9
	$\{\bar{1}10\}<110>$	2.0	11.2	*		**Total (%)**		**10.9**	**12.7**
	Total (%)		**59.8**						
pPv[d] 001 74 %	(010)[100]	4	*	1.1	pPv[e]	(010)[100]	1	*	22.4
	(010)[001]	4	*	9.8	010	(010)[001]	1	*	19.5
	(100)[010]	2	*	18.2	74 %	{011}[100]	10	*	2.9
	(100)[001]	2	*	8.9		(001)[100]	20	*	0.0
	(001)[100]	1	*	20.3		$\{1\bar{1}0\}<110>$	3	*	10.0
	(001)[010]	1.5	*	1.0		{111}<110>	50	*	0.0
	$\{1\bar{1}0\}<110>$	3	*	0.0		{111}<011>	50	*	0.0
	{110}[001]	4	*	0.8		**Total (%)**			**54.8**
	Total (%)			**60.1**					

*Indicates phase not present.
**MgO and CaPv activities taken from 010 model.

are minor phases, the impact on the macroscopic picture is not very significant. Also note that for Pv and pPv an artificial slip system {111}<10-1> had to be included with high CRSS to close the yield surface and prevent singularities in VPSC. VPSC proceeds by iterating between measuring the response of individual grains based on the input slip systems and the mean response of the bulk 'effective' medium and finds the consistent solution. Grains begin with an assumed spherical shape and are allowed to deform to a ratio of 3:1, after which only grain rigid rotation is allowed in agreement with previous models (Cottaar *et al.* 2014). Choosing a smaller ratio would lead to the texture developing earlier at the same strain rate, that is rigid rotation would occur sooner. This effect would increase the magnitude of anisotropy but not necessarily the signature of fast and slow directions. Furthermore, grains do not have the same shape, and the elongation varies due to the grain scale strain.

Also, no strain hardening is implemented. Although it is anticipated that the CRSS values would evolve with the P, T conditions in the lower mantle (Lin *et al.* 2019), we do not account for this in the present study because of lack of data. Furthermore, dynamic recrystallization is not taken into account in the current model even though it may be an important mechanism at lower mantle conditions. It can be incorporated in VPSC calculations (e.g. Wenk & Tomé 1999) but there is no experimental information to define controlling parameters.

From the resultant orientations after deformation along path-lines in steps, a 3-D orientation distribution (ODF) is calculated, and from it we obtain pole figures which are displayed in upper hemisphere projection (Figs 3d–e for a selected path-line), using the MTEX software package (Bachmann *et al.* 2010).

The pressure P (obtained through interpolation using PREM) and temperature T (obtained from the geodynamic model) are combined with a chosen Clapeyron slope for the Pv-pPv phase boundary of 11.2 MPa K^{-1} (Oganov & Ono 2004; Tsuchiya *et al.* 2004; Hirose *et al.* 2006) is applied to each path-line (illustrated for a single path-line in Fig. 4a) to find the location of forward and reverse phase transitions. If the transition conditions are met by a tracer crossing into the pPv stability zone, all Pv for that tracer transforms into pPv. During epitaxial phase transitions there are well-defined orientation relationships which are generally described by rotation matrices and there may be several variants which, especially under stress, are differently activated (e.g. Yue *et al.* 2019). Here we assume orientation relations described by Dobson *et al.* (2013) for the Pv–pPv transitions where the crystal c-axis is maintained but there are two variants of a-axes. An original orientation $\{\phi_1,\ \Phi,\ \phi_2\}$ (Bunge convention) splits into two orientations $\{\phi_1,\ \Phi,\ \phi_2 + \omega\}$ and $\{\phi_1,\ \Phi,\ \phi_2 - \omega\}$ with $\omega = 72.94^\circ$. After the phase transition, the new phase grains start from a spherical shape. We assume that both variants are equally active, regardless of orientation. Therefore, the number of orientations used in the VPSC calculations doubles during phase transitions, both Pv–pPv and pPv–Pv. To maintain the grain fractions of each phase, the number of MgO and CaPv grains are doubled again, resulting in 4000 grains at the end of the calculations.

2.3 Estimations of elastic properties and absolute velocities

To obtain elastic constants and seismic velocities of the 3-phase aggregate, we need to know elastic constants of single crystals. Here we use constants for pure end-members: MgO (Karki *et al.* 2000), CaPv (Kawai & Tsuchiya 2009) and Pv and pPv (Zhang *et al.* 2016) due to the availability of data at various P–T conditions. Where in previous models the evolution of the elastic constants with increasing P–T were not considered and a constant reference value was used (Cottaar *et al.* 2014; Wenk *et al.* 2011), in this study the elastic tensor components of each phase were interpolated to each P–T condition along the path-lines at every deformation step using the first and second derivatives in P and T. After each deformation step (which occurs at every recorded point along each path-line),

the resulting crystal orientations were combined with the respective elastic tensor through the self-consistent formalism used in VPSC to determine the elastic properties of the aggregate (Lebensohn *et al.* 2007). The self-consistent approach used here provides estimates of the aggregate elastic tensor with values that fall between the Voigt upper bound, which assumes the local strain in the aggregate is constant everywhere (i.e. iso strain) and the Reuss lower bound, formulated under the assumption that the local stress is constant everywhere (e.g. Kocks *et al.* 2000, pp. 303–305). At each time step along a path-line, the self-consistent aggregate elastic tensor is represented in a 6×6 matrix (21 independent values, C_{ij}), in Voigt notation, so that each data point in the model space is described by a set of 27 values ($\theta, \varphi, r, T, P, C_{ij}, \rho$). The number of data points in each of the 25 path-lines varies depending on the length of each path-line with values ranging from 350 to 580 data points per path-line resulting in over 10 000 data points throughout the model space. The radial anisotropy parameter ξ which compares the ratio of speeds of horizontally and vertically polarized shear waves was calculated from each aggregate elastic tensor at all points for both models using the following equation (Browaeys & Chevrot 2004).

$$\xi = \frac{V_{SH}^2}{V_{SV}^2} = \frac{\frac{1}{8}(C_{11} + C_{22}) - \left(\frac{1}{4}C_{12}\right) + \left(\frac{1}{2}C_{66}\right)}{\frac{1}{2}(C_{55} + C_{66})}. \quad (8)$$

Determining the aggregate isotropic velocities requires estimations of the density of the individual phases. We obtain the density of each phase at several pressures and temperatures from the literature also used to determine the elastic properties and it was then interpolated to all points within the model, together with each elastic tensor, based on pressure and temperature. As directly constraining the isotropic velocities, composition, and density are beyond the scope of this investigation, we compare the calculated isotropic velocities with PREM as a guide to the applicability of our model to observations, for example areas of faster and slower V_{Siso} than the 1-D average. The calculated absolute velocities from the model were compared to PREM and the change of *Vs* (d*Vs*) was calculated at each point along each path-line while the shear wave splitting (SWS) and radial anisotropy was compared to seismic observations of the lower mantle. SWS and V_{Siso} were computed using the MSAT software package (Walker & Wookey 2012) at selected points that sample different deformation geometries/ flow patterns along each path-line.

2.4 Addition of partial melting

In order to gain insight into the effects of partial melting that may occur at the base of upwellings, we compared the experimental data of Nomura *et al.* (2014) which looked at the melting conditions of a pyrolytic sample across the whole range of lower mantle conditions with the *P-T* conditions within our model to determine model locations where partial melting may occur along each path-line. A rough approximation of the properties of a silicate-based partial melt were implemented by incorporating a phase making up a volume fraction of 1–15 % of the aggregate that has the rough elastic properties of a silicate melt (Williams & Garnero 1996) and a shear modulus of 0. This phase was given the slip systems of a symmetric cubic crystal with critically resolved shear stress (CRSS) values of 0.01 (relatively no resistance compared to the other phases present) and an initial aspect ratio of 0.1 to simulate an equilibrium melt texture. The elastic properties were approximated under the assumption of isotropic elasticity (Babuska & Cara 1991).

The volume fraction of melt was tested at 1, 5, 10 and 15 %. An equivalent volume fraction was then removed from the Pv/pPv phase to accommodate the added 1–15 % of partial melt. Because the model space where partial melting is observed only varies in *T* by at most 50 K and roughly 20 GPa, and due to a lack of *P* and *T* derivatives at lower mantle conditions for a partial melt, we do not impose *P–T* variations in the elastic properties of the melt phase or the *P–T* effects to the density but rather directly impose the experimental values. As the volume fraction of melt increases the melt density contribution to the aggregate density would increase and would have to be taken into account.

Here we do not intend to constrain precise effects but instead we aim to observe a first order approximation of the effect from the addition of melt. Moreover, at low percentages of partial melting, the choice of volume percent partitioning was found to have little effect on the calculated signature of anisotropy from the aggregate. This is to be expected since the signature is dominated by the Pv/pPv phase where an expected loss of at most 15 % volume fraction still makes it 40 % more abundant than the second most prevalent phase, MgO. We are aware that this implementation is a rough approximation but argue that it provides insight into the effects on anisotropy at the onset of melting for low volume fractions. It also provides first order insight on the trends in isotropic velocities that could be expected in these high temperature areas, on the corresponding anisotropic signature of the aggregate, and also on the complicated signatures of anisotropy and velocities that may arise due to the presence of layering of phases atop a partial melt layer near the CMB.

3 RESULTS

3.1 CPO evolution within the slab

The CPO evolution within the slab is dictated by the evolving strain rate as the slab moves into different flow regimes. For instance, during downwelling we find an average equivalent strain rate of $\sim 1.15 \times 10^{-13}$ s^{-1} and increasing by $\sim 1.6\times$ as the slab turns along the CMB (Fig. 3e), which leads to a rapid evolution of the CPO within the aggregate. The strain rate reaches a minimum once the slab material meets the pile but is then forced into upwelling flow and the rate of strain dramatically increases to $\sim 8 \times 10^{-13}$ s^{-1} ($38\times$ increase at a depth of 2296 km, ~500 km above the CMB compared to the minimum value as the slab meets the pile) and then decreases as the material travels upward away from the CMB. Fig. 5 shows the crystal preferred orientation (CPO) developed along a selected path-line for both tested models at three important locations within the slab: (1) just before the Pv–pPv transition (first row), (2) during horizontal flow along the CMB (rows 2–3) and (3) during upwelling (post reverse pPv–Pv transition in rows 4–5). Both models are identical except for the dominant slip systems in the pPv phase. The initial Pv texture shows a strong (100) texture just prior to the phase transition ~8 m.r.d. which is immediately dispersed once the phase transition is initiated. After the phase transition occurs (signified by horizontal black lines in Fig. 5), Model 001 develops a steady increase of an (001) maximum orthogonal to the material flow direction due to 'textural inheritance' from the (001) maximum developed in the parent Pv phase. While Model 010 shares an (010) distribution similar to that of Model 001, *albeit* weaker, the normals to the (001) and (100) lattice planes are nearly orthogonal between the two models. The secondary cubic phases MgO and CaPv both develop CPO in a girdled fashion with maxima nearly aligned with the flow direction attaining a maximum of ~5 m.r.d. during downwelling,

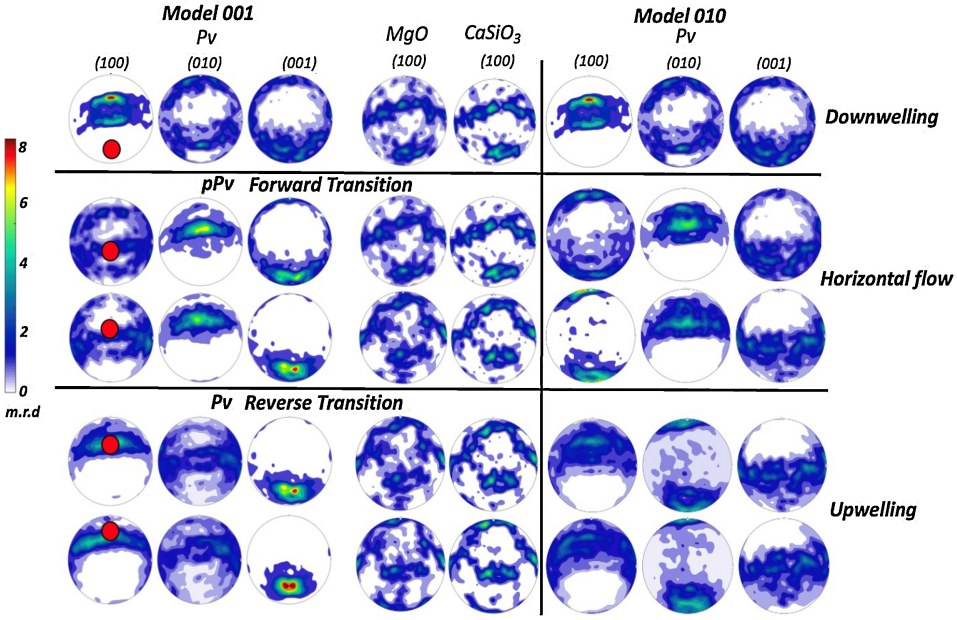

Figure 5. Deformation of Pv/pPv + MgO + $CaSiO_3$ for Model 001 and Model 010 at locations just before and after the forward and reverse phase transitions path-line 3 in Fig. 9. Textures are represented as equal area upper projection pole figures and shown in a scale of multiples of random distribution (m.r.d). The CMB is horizontal in all images. Flow direction is indicated by red dots in the first column and is the same across all pole figures.

that is maintained throughout the simulation. Table 2 shows the slip system activity for each phase as a percent which defines the relative contribution of each slip system to the total shear. The minor phases are found to be slightly more active in Model 010 making up 45.2 % of the slip activity compared to 39.9 % in Model 001 (Table 2). After the reverse pPv–Pv phase transition, the (001) texture is again inherited into the daughter Pv phase and continues to increase in strength as well as rotate with the flow direction for Model 001, reaching a maximum of ∼10 m.r.d. By contrast Model 010 sees an initial dispersion of CPO just after the reverse phase transition and only reaches a maximum of ∼4–5 m.r.d for any slip system in the volumetrically dominant Pv phase during upwelling.

3.2 Shear wave anisotropy

Given the weakly anisotropic elastic structure of the dominant Pv phase, we find that the initial downwelling part of the slab appears largely isotropic. The forward Pv–pPv transformation occurs over a range of 50 km (2550–2600 km) and leads to an abrupt jump in magnitude of both shear (∼1.5 % on average, 3.5 % max) and compressional (1.5–4.0 %) wave velocities (Fig. 6). This recorded jump in isotropic velocities is accompanied by the appearance of a lower symmetry anisotropy than the generally assumed vertical transverse anisotropy (VTI, Fig. 7) with $V_{SH} > V_{SV}$ (i.e. $\xi > 1$, Figs 8a and b), with ξ steadily increasing as the slab proceeds along the CMB, in both models, from a value of 1–3 % . ($\xi = 1.01 - 1.03$) to a maximum of ∼6 % in the deepest parts of the slab, as it impinges on the CMB. Horizontal fast axis orientation (also region highlighted in red for presence of pPv in Figs 8(c) and (d) continues throughout the region of horizontal flow along the CMB, in agreement with seismic observations in regions of slab graveyards (Panning & Romanowicz 2006; Sturgeon *et al.* 2019). Due to the 3-dimensional nature of the geodynamic model, we are able to investigate deformation arising from the heterogeneous strains imparted along different paths through the thickness of the slab such as edges, where spreading

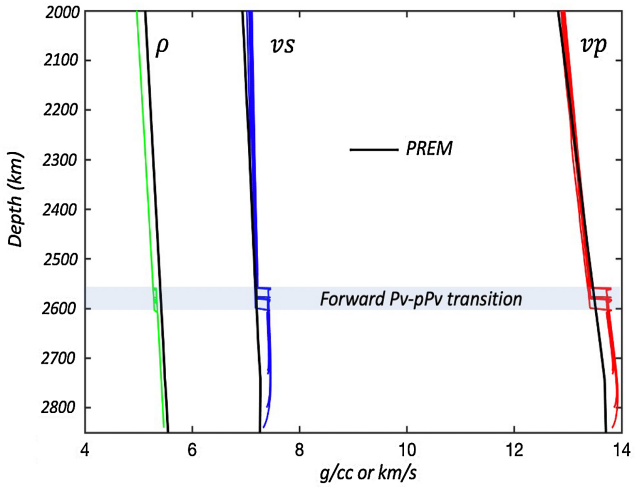

Figure 6. Comparing isotropic velocities and density of the model aggregate with composition and PREM. Model isotropic shear (blue) and compression (red) wave speed as well as density (green) compared to PREM (black). The range of the Pv–pPv phase transition represented by grey shading and clearly demarcated by the abrupt jump in all three parameters at ∼2560 expanding to just past 2600 km. Errors in density below 2000 km range from 0.4 to 1.5 % compared to PREM. Units g cc^{-1} are for densities and km s^{-1} for velocities.

and rolling occur as the slab impacts and traverses the CMB near the edges of the simulated LLSVP resulting in varying depth and azimuthal anisotropic signatures. Here we find the plane of highest shear wave anisotropy has a tilted axis of symmetry (tilted transverse anisotropy (TTI)) with an inclination of up to ∼20–30° from the radial direction (vertical, Fig. 9, #3) similar to that observed at D" depths beneath the Caribbean (Garnero *et al.* 2004. Included in Fig. 8(b) is also a path-line (1) that fails to meet the phase transition conversion criteria and therefore retains the Pv phase. The Pv layer atop the slab exhibits a vertically oriented fast *S*-wave propagation

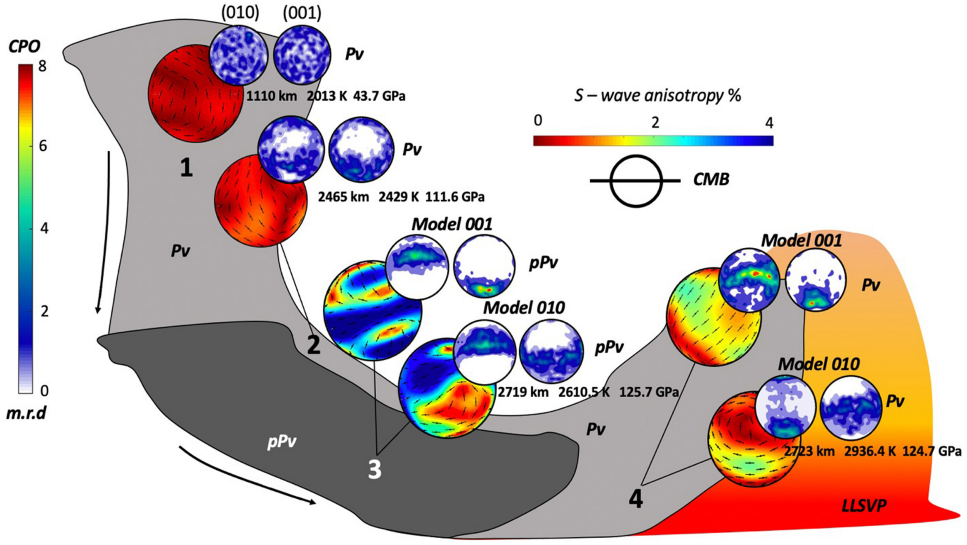

Figure 7. Sketch of subducting slab highlighting the plastic deformation induced anisotropy and the presence of Pv (light grey) or the pPv (dark grey) in different areas of the slab. Plastic deformation shown as upper hemisphere pole figures (units of multiples of random distribution, m.r.d) for the Pv/pPv phase along with associated shear wave anisotropy of the aggregate as 3-D projections from different path-lines, each sampling different areas of the slab (1–4). Black ticks in velocity projections indicate fast shear wave polarization direction. Locations (3, 4) show variations between Model 001 and Model 010. The CMB is horizontal as shown by the diagram upper inset. The hotter region (labelled LLSVP) and shown in shades of orange, corresponds to the pile shown in Figs 3(a) and (c). The top part of the slab (2) is colder, retaining the Pv phase. At the border of the hot pile, the reverse pPv to Pv occurs in the deeper parts of the slab first, so a small sliver of pPv becomes sandwiched between the newly reverted Pv beneath (2690 km to the CMB in some areas), and the never converted Pv above.

direction orthogonal to the horizontally oriented fast *S*-wave of the underlying pPv.

Several studies (Williams & Garnero 1996; Simmons & Grand 2002; Yuan & Romanowicz 2017) have suggested that a small percentage of partial melt could explain the strongly decreased velocity signatures of ultra-low velocity zones (ULVZs). We investigated these effects in our model through the methods described in Section 2.4. Rough estimates on the elastic parameters of a silicate-based melt are incorporated to the aggregate at the determined locations. The onset of partial melting in the model was found to occur in the deepest portion of the slab near locations with the reverse pPv–Pv phase transition. We find the presence of as little as 1 % melt results in a ∼2.5 % decrease in *P*-wave velocity and ∼4 % decrease in *S*-wave velocity compared to the same path-lines without partial melting added. Increasing the melt per cent to 15 % leads to reductions in V_S and V_P of ∼18 and 7 %, respectively at the base of the upwelling (Figs 10 and 11). We observe a very small deviation in the direction of fast polarization in either model, but a strong increase in the amplitude of anisotropy (Fig. 12).

As slab material approaches the edge of the dense hot pile, the increase in T initiates the reverse pPv–Pv transformation, which occurs at a range of depths depending on location in the model, but generally deeper (2595–2835 km) than for the forward transition, as anticipated due to the larger T near the edge of the hot pile. This is where significant differences between the two pPv models emerge in both texture development as well as anisotropy (Figs 5–7): for Model 010, the fast axis direction with relatively larger SWS strength (∼1.0–3.0 %) remains horizontal after the reverse transition and the trend continues during the upwelling; Model 001, on the other hand, shows a complex pattern of mixed horizontal and vertical fast axis directions after the reverse pPv to Pv transition with ∼2.0 % of SWS strength, and a tilted fast axis with 1.0–2.0 % SWS strength in the upwelling segment (Fig. 7). Interestingly, a triple layering (Fig. 7) of varying shear wave polarization as well as isotropic velocities due to double crossing of the pPv phase boundary occurs over a 300 km depth range in Model 001. While the same triple layering of phases occurs in Model 010, the extreme reversal in fast propagation directions between layers is not as apparent. Also, Model 010 only presents small patches of $V_{SH} < V_{SV}$ at the base of the upwelling (red areas in a prevailing pattern of $V_{SH} > V_{SV}$ (blue areas) in the upwelling region). The latter is inconsistent with available seismic observations (e.g. Long 2009; Romanowicz & Wenk 2017).

4 DISCUSSION

4.1 Distribution of Pv and pPv in the lowermost mantle

By including cubic MgO and CaPv as well as both direct and reverse phase transition from Pv to pPv, we gain a more realistic representation of the complex aggregate thought to exist in the lowermost mantle. Furthermore, an interesting observation that arises due to the temperature variations in the model is the depth dependence of the Pv–pPv and pPv–Pv phase transitions. While the forward transition is found to only vary over ∼40 km in this model, the changes in elevation of the reverse transformation are much larger, ranging over a ∼200 km depth and 15° of colatitude along the slab's path (Fig. 13). This results in a situation where we find a ∼100–250 km wedge of lower-than-average isotropic velocity Pv on top of the CMB at the edge of the simulated pile located beneath the faster than average pPv phase, due to a double crossing of the Pv–pPv phase transition (Hernlund *et al.* 2005). This unique feature causes a triple layering of differing shear wave anisotropies (Fig. 7) as well as isotropic velocities. The presence and extent of this feature is ultimately dependent on the value of the Clapeyron slope chosen to represent the locations of the forward and reverse phase transitions (Fig. 4a). We also find path-lines that fail to convert to pPv altogether and constitute the top layer of the simulated slab. These

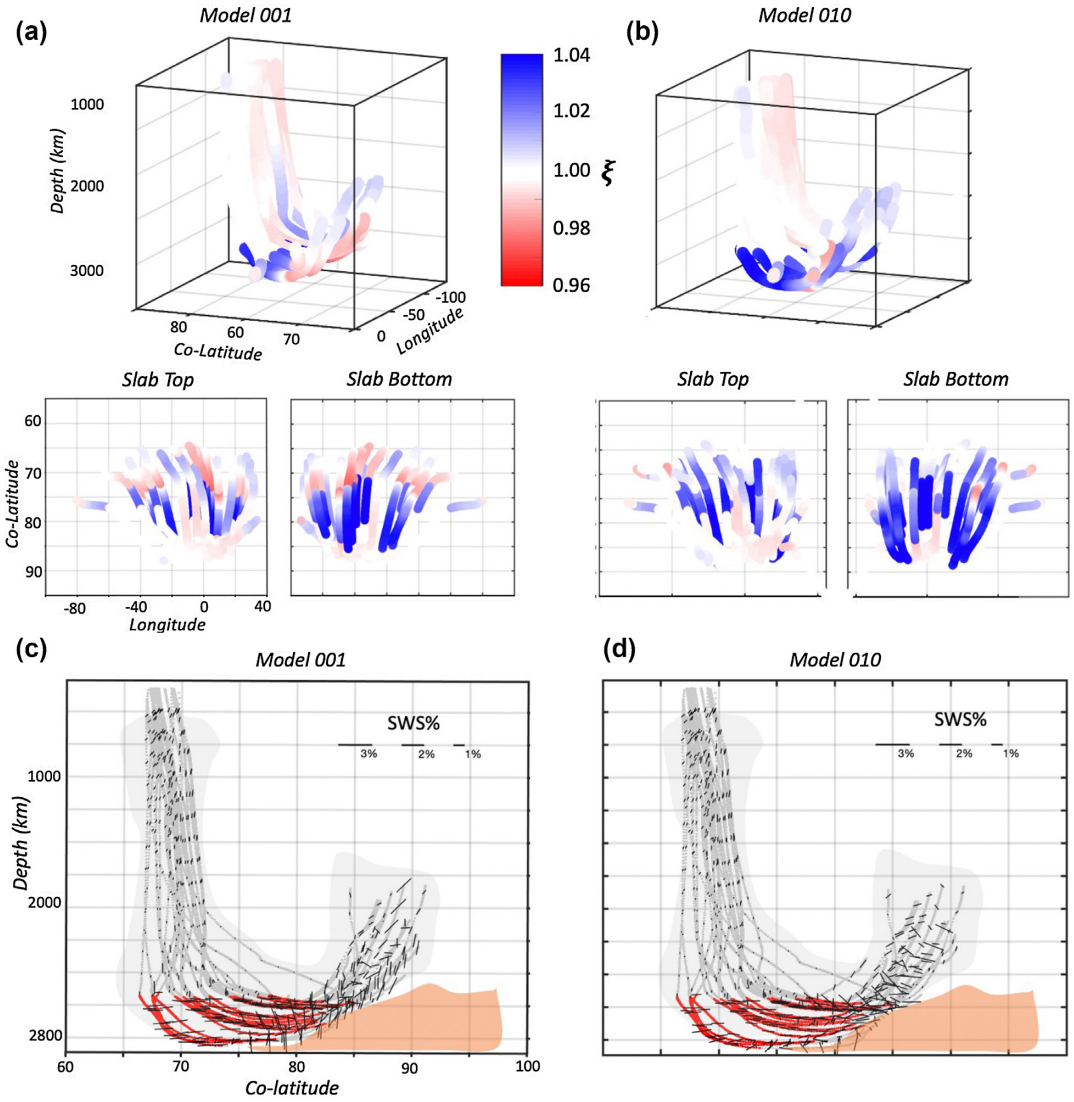

Figure 8. Spatial distribution of radial anisotropy and shear wave splitting. Top panels: radial anisotropy parameter [$\xi = (V_{SH}/V_{SV})^2$] computed along each path-line for Model 001 (a) and Model 010 (b) (25 total path-lines), showing oblique view highlighting entire slab path (black arrow indicates slab flow direction) and views from top and bottom of the slab, respectively, for both models. Bottom panels: Shear wave polarization directions for waves propagating at grazing incidence to D" for (c) Model 001 and (d) Model 010. Red paths highlight areas where the pPv phase is present. Orange areas indicate areas of increased temperature at the base of the upwelling. Black ticks indicate the fast polarization direction scaled by per cent. Incident seismic wave direction is into the page.

path-lines (depicted by path-line 1 in Fig. 9) show the effect of absence of the pPv transition and lead to very weak but vertically polarized shear waves being the fastest. This is at odds with previous studies (Cottaar *et al.* 2014) but this discrepancy is understandable due to the choice of dominant slip systems in the Pv phase with (001) dominant (Wenk *et al.* 2011) compared to a mix of (001) and (100) in this study based on Mainprice *et al.* (2008). Furthermore, in Cottaar *et al.* (2014) the intrinsically dense layer used in the current model was not present. This addition leads a drastic change in the local dynamics between models near the CMB. For instance, once the slab meets the CMB, without the thermochemical pile acting as an initiating point for upwelling the slab would have been able to spread further along the CMB. The lack of the pile would also affect the extent and location of the reverse pPv–Pv transition we observe in this model.

The viscosity of the pPv phase has also been debated, and a viscosity either greater (Karato 2010, 2011) or weaker (Ammann *et al.* 2010) than that of Pv has been proposed, which may have opposite effects on the dynamics in the D" and CMB regions. In the case of 'weak' pPv, Li *et al.* (2014) and Nakagawa & Tackley (2011), showed that slab material that reaches the CMB would spread more easily. In our model, the incorporation of a 'weak' pPv could potentially lead to a higher strain rate which would allow for a more rapid texture development of the local minerals. The weak pPv would also lead to a thinner thermal boundary layer beneath subduction regions above the CMB, which would widen the region of pPv stability in our model, since we include the reverse pPv–Pv transition and the amount of Pv along the CMB would possibly decrease. As mentioned above, we find that the newly formed Pv at the CMB has an anisotropic signature with $V_{SV} >$

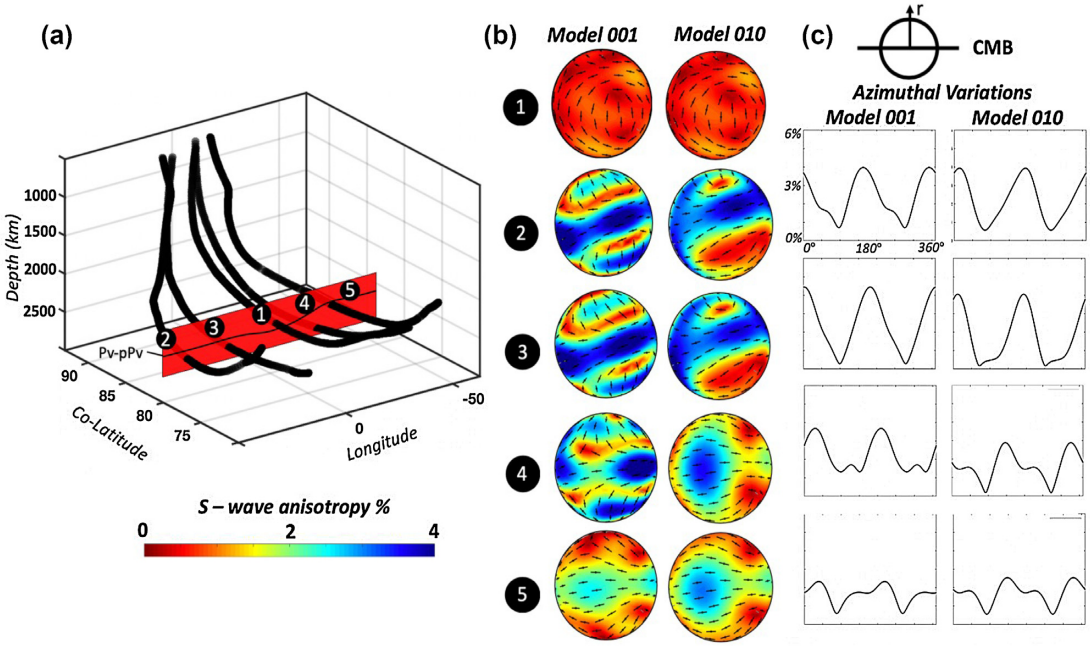

Figure 9. Shear wave and azimuthal variations for Model 001 and Model 010 through transverse slice of slab at 80° colatitude (green barrier) during slab transit along the CMB. (a) View of 5 selected path-lines passing through the traverse slice of the model slab (red) as well as black line to guide reader to Pv/pPv phase transition boundary. (b) 3-D shear anisotropy projections for the aggregate with (001) and (010) slip dominant in the pPv phase when present) for corresponding path-lines with fast direction polarization shown as black ticks, with flow direction out of page. Note that path-line (1) fails to convert to pPv and retains the Pv phase in both systems. (c) Azimuthal variations in shear wave velocity magnitude in the horizontal plane. The CMB is horizontal and radial direction is north in all images as depicted in the upper right inset. Flow direction is out of the page.

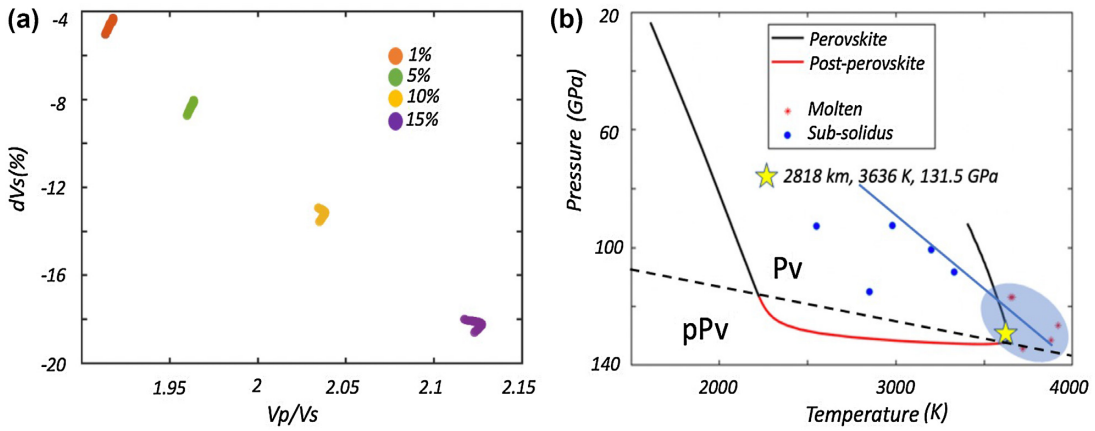

Figure 10. Location and effects of partial melting on shear wave anisotropy and isotropic velocities showing (a), a plot of dV_{Siso} in per cent deviation from PREM against the ratio of V_P/V_S for the isotropic velocities with various amounts of partial melting showing the widening gap between V_P and V_S with increased melt per cent. (b), Pressure-temperature trace of a selected path-line reaching the deepest level of the lower mantle at conditions of possible partial melt determined by Nomura *et al.* (2014). Blue circles represent data points taken from this study where no partial melting was detected experimentally (subsolidus). Red stars indicate the presence of partial melt (molten). Shaded area (grey) shows location of possible melt conditions with blue solid line the liquidus from Nomura *et al.* 2014, in the model and yellow star shows location of velocity projections in Fig. 9(b).

V_{SH}. If Pv was less abundant along the CMB, the size of patches of $V_{SV} > V_{SH}$ would decrease at the cost of patches of $V_{SH} > V_{SV}$. This fact could be used in future models as a constraint on the amount of pPv present along the CMB. The thinner thermal boundary layer above the CMB would also reduce the size of area along the CMB where we would find partial melting, at least under our tested conditions. This would therefore have the effect of reducing the size of exceptionally low velocity patches found at the base of upwellings.

4.2 Effect of phase transitions and partial melting on deformation and shear wave anisotropy

Along the lines of previous studies, we aim to identify models that are consistent with the long wavelength seismic anisotropy structure observed in D". In previous studies (Wenk *et al.* 2011; Cottaar *et al.* 2014), we were able to provide evidence that dominant slip on 001 or 010 in a pPv+MgO+CaPv aggregate caused by convection-driven shear deformation could provide an explanation for the anisotropic signatures of D". Those same studies showed that Pv alone as well

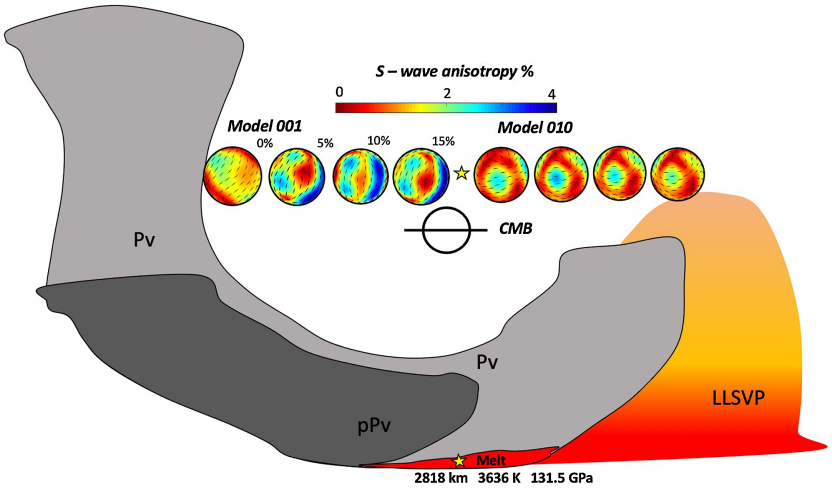

Figure 11. Shear wave anisotropy resulting from various amounts of partial melting as 3-D projections of shear wave anisotropy for the addition of 0, 5, 10 and 15 % partial melting at the base of the model slab near the edge of the simulated pile labeled LLSVP. Red section near the bottom of the slab depicts a section containing partial melt. Star indicates location shown by star in Fig. 10(b). CMB is horizontal in all images.

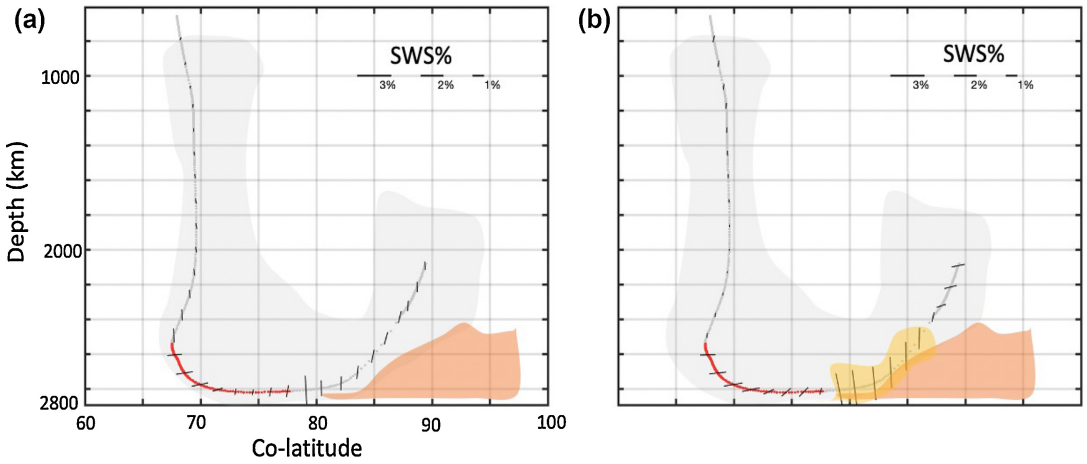

Figure 12. Comparing shear wave polarization directions for waves propagating at grazing incidence to D" for a representative path-line, (a), without partial melting and (b), with 1 % partial melt for Model (001). Black tics indicate the fast axis direction scaled by %. Red path marks the presence of pPv. The area of the slab where partial melt is present is shown in yellow, while orange represents increased temperature at the base of the upwelling. All incident wave propagation directions are into the page. Brown structures represent dense pile and orange structure highlights section of path-line with melt present.

as dominant slip in (100) in the pPv phase could not reconcile the bulk seismic anisotropy signatures in the lowermost mantle and therefore we do not include those systems here. A more recent study performed by Tommasi *et al.* (2018) provided further evidence for (010) dominant slip by utilizing 2-D corner flow models similar to those of Wenk *et al.* (2011). They were able to show that an (010) dominant pPv phase was capable of explaining both a horizontal (to sub horizontal) fast shear wave polarization in D" as well as a flow-directed fast direction in upwelling areas. A key aspect of the current study is the temperature dependence on the spatial presence of the pPv phase, and the corresponding phase transition which was not taken into account by Tommasi *et al.* (2018). In our model, pPv cannot exist thermodynamically in the hotter regions near the edges of the simulated LLSVPs, and therefore we conclude alternate explanations are needed to describe the observed anisotropy at the base of upwellings.

The current model corroborates the findings of Tommasi *et al.* (2018) and Ford & Long (2015) that dominant (010) slip in the pPv phase (our Model 010) can explain the anisotropic signature during the transition from downwelling to horizontal flow along the CMB but cannot reconcile signatures seen in areas of upwelling. Nowacki *et al.* (2010) also tested (001) and (010) dominant slip in pPv through comparison of the orientation of shear planes and slip directions of the two systems and the measured differential shear wave splitting of S and ScS phases passing through D" beneath the Caribbean. There they found the strongest correlation between (001) dominant slip in pPv but could not rule out (010) without further investigation. By incorporating the three flow regimes here (downwelling, horizontal flow, and upwelling) we are able to draw a clear distinction between (001) and (010) dominant slip. The difference between the two models tested here is due to the textural (001) inheritance across the pPv–Pv phase transition (Dobson *et al.* 2013) that occurs at the base of the upwelling section in Model 001, which leads to an increase in 001 texture intensity during upwelling flow (up to >10 m.r.d), aligning the aggregate fast direction of anisotropy, on average, near the material flow direction (Figs 7and 8c). In contrast, in Model 010 there are two abrupt partitions of slip activity (Fig. 14b). At the forward Pv–pPv transition we see a

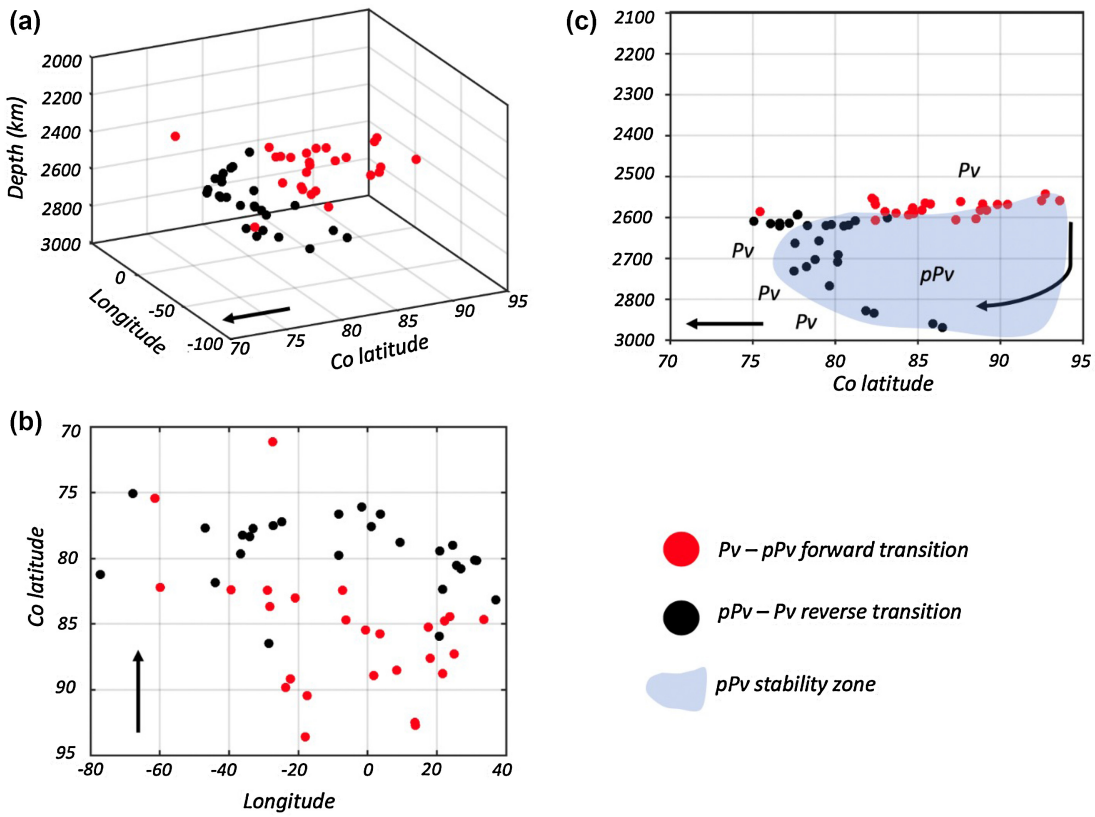

Figure 13. Spatial variation of forward (red dots) and reverse (black dots) phase transitions in the slab. 3-D visualization in a with 2-D in (b) and (c). When viewed from above (b) the spread of the reverse pPp–Pv transition is clearly identified. Grey area in c shows the pPv stability field within the slab highlighting the deeper penetrating path-lines reverting to Pv (near 90° Co latitude) compared to shallower paths (black dots at 75–80° Co latitude). Slab flow direction is shown by black arrows in all images.

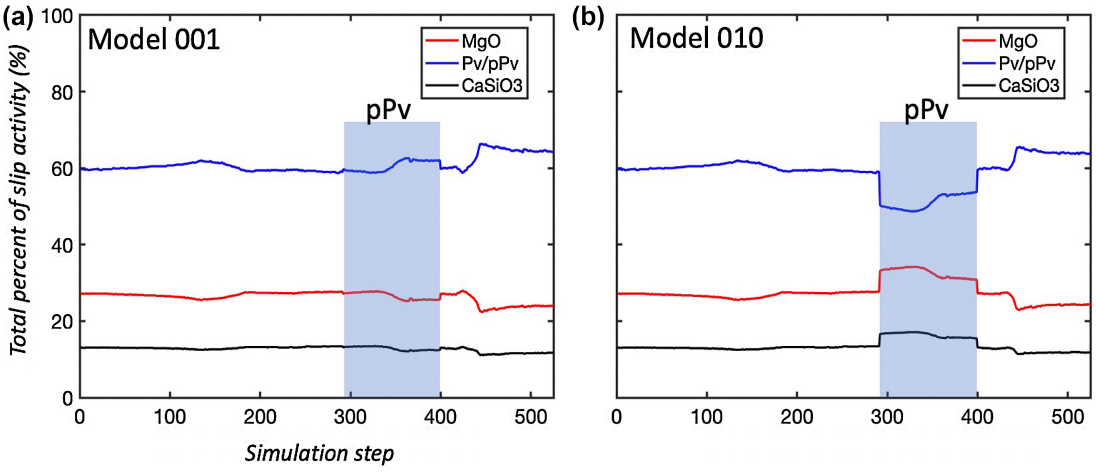

Figure 14. Strain partitioning between Pv/pPv (blue) and MgO (red) and CaPv (black) measured as slip system activity (%) which represents the sum of relative amounts of shear contributed by each phase per simulation step for path-line 3 in Fig. 7 for (a) Model 001 and (b) Model 010. Shaded blue area represents the section of the path-line the pPv phase. Step 0 represents the start of the simulation and step 525 is at the end. Interestingly, in Model 010, there is sudden transfer of slip activity from Pv/pPv to MgO and CaPv at the phase transition points. This feature is also present in Model 001 but is suppressed due to the textural inheritance in the pPv phase.

partition of ∼15 % of slip activity to the weaker MgO and CaPv phases due to the fact that pPv in Model 010, is in an unfavourable geometry for slip on its dominant mode (010) but in two directions [100] and [001]. But it is clearly seen that after the transition the (001) texture from the original Pv remains (Fig. 5 columns 3 and 8). A second partition happens after the reverse pPv–Pv transition, this time in the opposite direction and the newly formed Pv phase abruptly absorbs ∼8 % of the slip activity from the minor phases which is understandable seeing as the Pv in this study can accommodate slip on the three major planes (100) (010) or (001) in various directions. Ultimately, this leads to a substantially weaker preferred orientation in the Pv phase in Model 010 as well as to (010) and

(001) distributions orthogonal to those seen in Model 001 (Fig. 5), ultimately leading to the fast direction in Pv remaining near parallel to the CMB. This results in the dominantly horizontal fast direction of anisotropy, that is orthogonal to the flow direction during upwelling, at odds with seismic observations in the LLSVPs (e.g. Nowacki *et al.* 2011; Romanowicz & Wenk 2017). This is further illustrated by visualizing the lateral and depth dependent anisotropic structure in D" produced by the model as a whole similar to that done in 2-D by Wenk *et al.* (2011). If the effect of textural inheritance we find in Model 001 does occur in the lower mantle, then it would follow that the strength of anisotropy in D" due to pPv would be modulated by the amount of (001) texture that occurs in the precursor Pv phase, that is strong (001) texture in Pv would lead to a strong (001) starting texture in pPv, and therefore a strong anisotropic signature emanating from a pPv dominated aggregate. This scenario could explain the variation in strength of anisotropy in areas of suspected pPv. Also, including the *P–T* dependent phase transition, we find a complicated mix of vertically and horizontally polarized shear waves dominating in the hottest regions at the base of the slab (bottom of Fig. 8), where lateral temperature variations induce reversion to Pv in some locations but not others, a feature not seen in our previous studies but consistent with seismic observations (Romanowicz & Wenk 2017; Nowacki *et al.* 2011). Beyond these differences however, and although we introduce more realistic complexity, even when including the Pv–pPv–Pv transition pathway, our Model 001 correlates to the pPv C model proposed in Cottaar *et al.* (2014), with fast shear propagation directions aligning near the flow direction through all three flow types of the model (downwelling, horizontal flow, upwelling).

We also tested a case in which the phase transition does not follow the topotaxial relationship of Dobson *et al.* (2013) but instead its occurrence results in randomization of the newly introduced grains in the pPv (or Pv). Because Pv (or pPv) heavily dominates the volume fraction of the aggregate, this has the overall effect of decreasing the magnitude of the calculated anisotropy to near isotropic, with the anisotropy increasing near the end of horizontal flow, which is then removed by the randomization once again at the reverse Pv–pPv transformation at the base up upwelling. Both results are in disagreement with the magnitudes of anisotropy observed in D".

We not only investigate the anisotropy developed along individual path-lines, but also collapse each deformed aggregate elastic tensor into its scalar $\xi = (\frac{V_{SH}}{V_{SV}})^2$ value at over 10 000 points within the model which allows for a volumetric mapping of the radially anisotropic structure of the slab in Model 001 and Model 010 (Fig. 15). This approach provides a volumetric image of the anisotropic structure of the slab with clear demarcations in the change from $V_{SH} > V_{SV}$ (blue) during horizontal flow along the CMB to areas of $V_{SV} > V_{SH}$ (red) during upwelling flow for Model 001 (a–d) while Model 001 only shows small patches of $V_{SV} > V_{SH}$ in those areas (Fig. 15h).

As for the secondary phases, although MgO exhibits strong shear wave anisotropy (Marquardt *et al.* 2009), and at 19 % volume fraction accommodates between 25 and 35 % of the strain in this model, while the overall signature of anisotropy is dictated by the abundance of the Pv/pPv phase, which makes up 73 % of the aggregate and the fact that in cubic MgO, velocity values are spread in three vertically identical directions. The resulting patterns of shear wave anisotropy we find here in D" are very similar to those calculated in previous models (Wu *et al.* 2017; Zhang *et al.* 2016) when accounting for 001 slip in the pPv phase. The addition of the also cubic CaPv appears to reduce the amplitude of anisotropy, compared to the case where only a combination of Pv and MgO was considered (Cottaar *et al.* 2014) but has a minimal effect otherwise.

In our model, thermal variations at the base of the pile meet the conditions necessary for partial melting to occur, which then acts to decrease the absolute velocities for both *P* and *S* waves (Fig. 10) while increasing the magnitude of anisotropy of the plastically deformed aggregate. This is consistent with seismic observations near the edges of LLSVPs at D" depths (Lynner & Long 2014) using SK(K)S observations along the edge of the African LLSVP. While splitting was observed near the edges, that study found little or no splitting for phases that pass through the LLSVP, also in agreement with Cottaar & Romanowicz (2013). This led the authors to infer that deformation may only occur along the LLSVP edge while the interior possibly remains relatively undeformed. While in our model, we do not sample the interior of the simulated LLSVP but instead concentrate only on the slab material near the edge of the pile, that is deflected upward by its presence, future models should incorporate anisotropic signatures from material surrounding the slab. This will allow further investigation and comparison between the upwelling slab material and the signature arising from the pile interior.

4.3 Limitations

While this revised model incorporates many new features, still, our model relies on several simplifications and assumptions. The geodynamic model assumes a homogeneous isotropic viscous medium and does not take texture evolution into account nor does the geodynamic model include effects of partial melting or hydrous phases. CPO is introduced *a posteriori* based on the recorded velocity gradients. In one of the first studies of texture evolution in a convecting mantle with finite element methods (Blackman *et al.* 1996; Dawson & Wenk 2000) it was illustrated that plastic anisotropy can have a large effect on convection, causing local curling and stagnation. In the future one should consider introducing plastic anisotropy into the geodynamic model. Even if Pv in the lower mantle is elastically fairly isotropic, our modelling shows that it is plastically very anisotropic, with strong texture development (e.g. Fig. 4 top).

We assume that the mantle is a homogeneous medium of PREM composition. This is clearly a simplification as recent geochemical investigations suggest, with regions of peridotitic composition but others of eclogitic composition (e.g. Gleeson & Gibson 2019; Gleeson *et al.* 2020) and also a mixed composition of high-density mid-ocean ridge basalt (MORB) and lower density harzburgite which causes slab rotation, placing the MORB layer along the CMB (Tackley 2011). Some studies have mentioned evidence for minor phases in the deep Earth such as the hexagonal H-phase (Zhang *et al.* 2014) resulting from the Fe disproportionation in iron bearing Pv to an iron depleted Pv + iron rich H-phase, or seifertite (Zhang *et al.* 2016) coexisting with pPv. Our model incorporates only pure end-member and dry, phases, while Nomura *et al.* (2014) conducted their study on a sample containing iron as well as 400 ppm H_2O. The partitioning of water could affect the ease of deformation in the dominant Pv and pPv phases, although investigations into hydrolytic weakening of mantle minerals (Muir & Brodholt 2018) found that at low ppm (sub 200 ppm) water tends to partition to the Pv phases, while at higher amounts, water should move to the CaPv phase. Also, the use of pure end-member phases neglects the effects of phenomena such as electronic spin transitions observed in (Mg,Fe)O at lower mantle conditions (e.g. Antonangeli *et al.* 2011; Yang *et al.* 2015;

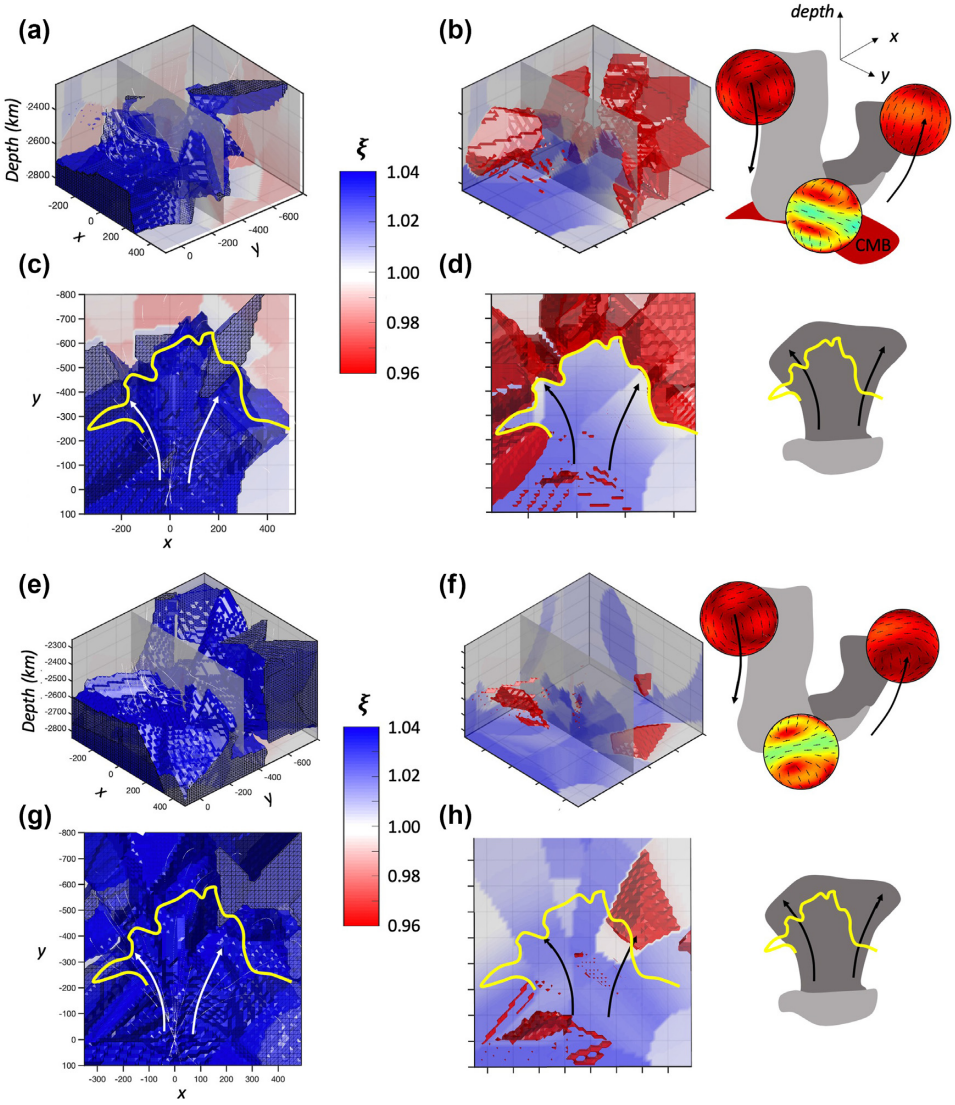

Figure 15. Volumetric mapping of radial anisotropic parameter ($\xi = (V_{SH}/V_{SV})^2$) within the slab for Model 001 (a–d) and Model 010 (e–f) showing (a), an oblique view of slab volume showing $\xi > 1$ indicated by iso-contour of constant $\xi = 1.02$ (2 % V_{SH} fast) and (b) area of slab with $\xi < 1$ indicated by iso-contour of $\xi = 0.98$ (2 % V_{SV} fast). (c–d) viewed from above with the pPv–Pv reverse phase transition demarcated by yellow line. Figure bound values indicated by the color. Cartoon slabs on the right guide the reader about slab flow direction with 3-D velocity projection of *S*-wave anisotropy shown for each flow section for both models. Vertical axis shows depth in km while the colatitude (y) and longitude (x) were converted to Cartesian coordinates during the meshing process.

Wu 2016) which can have a large effect on the resultant anisotropy in this phase, as well as variations in density which would affect the isotropic velocities. These compositional complexities have not only an effect on plasticity but on physical properties such as density and elasticity.

Texture simulations with VPSC assume that plastic deformation occurs purely by dislocation glide. Without constraints on the amount of contribution from non-rotational deformation mechanisms in the lower mantle, we assume that only 50 % of the strain causes crystal rotations. But other mechanisms are ignored such as diffusion resulting in grain growth which is particularly significant in polyphase materials as was explored experimentally (e.g. Marquardt & Miyagi 2015; Chandler *et al.* 2021) and with finite element models (Kasemer *et al.* 2020). For example, in Pv–MgO aggregates softer MgO appears to develop minimal CPO. This leads us to the mechanism of dynamic recrystallization—nucleation of new grains and grain growth—which likely plays a significant role at lower mantle conditions. It was introduced into the VPSC model (e.g. Wenk *et al.* 1997; Wenk & Tomé 1999) and applied to upper mantle convection (Blackman *et al.* 2002), but so far never used for lower mantle models, largely because of lack of experimental data.

Furthermore, although we incorporated phase-transformations into the deformation model, the associated energetic effects (Oganov & Ono 2004) as well as the choice of Clapeyron slope of this transition could also have significant effects on the local temperature and viscosity and therefore strain rates and active deformation mechanisms within the slab. Further studies are needed to address these technically challenging questions, coupled with more detailed measurements of seismic anisotropy at the edges of and within mantle upwellings.

Our incorporation of melting remains a first approximation and includes two large assumptions (1) We do not account for any increased density effect due to Fe that may occur in the melt and which may increase any velocity reductions we suggest in our model and (2) when testing various amounts of melt in our model we do not adjust the density of the aggregate. We feel this assumption is valid for less than 5 % of melt as it is anticipated that the density of a pure end-member melt at these conditions would have a similar density to that of the surrounding aggregate and fluctuations of a few % or less would have little effect on the density contribution to the calculated anisotropy. Future geodynamic models which include the addition of partial melting would however have the effect of lowering the viscosity where melt is located which could act to increase the strain rate locally imparting accelerated effects on texture development as well as the calculated anisotropy of the aggregate.

5 CONCLUSIONS

We have modelled the effect of both forward and reverse Pv–pPv phase transitions and partial melting on seismic anisotropy in a subducting slab being deformed along the CMB as well as areas of upwelling. Our study provides insights on how phase transformations in the Pv–pPv system and temperature variations related to dynamic flow patterns contribute to explaining the observed seismic anisotropy patterns in the deep mantle. We find that incorporating a texture inheritance for the forward and reverse Pv-pPv phase transitions is significant for interpreting observations of seismic anisotropy in D". We argue that Pv alone cannot produce the combination of isotropic shear velocities and anisotropic signatures seen in D" and therefore another phase or factor must contribute. We find that only a model with (001) dominant slip for pPv provides results consistent with a strong but complicated anisotropy, with $V_{SH} > V_{SV}$ in regions of faster than average isotropic *Vs* (e.g. graveyards of slabs), a tilted fast axis of anisotropy near the borders of the LLSVPs and flow-aligned or absent anisotropy as observed in hotter than average regions of upwelling.

ACKNOWLEDGEMENTS

We acknowledge support from NSF (EAR 1343908 and EAR1464014) and DOE (DE-FG02-05ER15637). BC was awarded a doctoral fellowship at the Advanced Light Source of Lawrence Berkeley National Laboratory (LBNL). BC would also like to thank William Davis for the very constructive conversations in interpreting various parts of the model, Carlos Tomé for discussions pertaining to the VPSC code and Allan McNamara for initiating the geodynamic model used in this study. We would like to thank Sanne Cottaar and Roman Vasin for the insightful conversations and guidance in progressing the model. We are appreciative for comments by reviewers which helped us to improve the manuscript.

Author Contribution: All authors contributed to the vision and design of the project and to the resulting analysis. BC developed the codes for visualization and performed the mineral physics and seismological calculations with the assistance of LC. ML conducted the geodynamic modelling experiments. All authors contributed to writing the paper.

COMPETING INTERESTS

The authors declare no competing interests.

DATA AVAILABILITY STATEMENT

The data underlying this paper will be shared on reasonable request to the corresponding author.

REFERENCES

Ammann, M.W., Brodholt, J.P., Wookey, J. & Dobson, D.P., 2010. First-principles constraints on diffusion in lower-mantle minerals and a weak D′′ layer, *Nature,* **465,** 462–465.

Amodeo, J., Carrez, Ph., Devincre, B. & Cordier, P., 2011. Multiscale modelling of MgO plasticity, *Acta Mater.,* **59**(6), 2291–2301.

Antonangeli, D. *et al.*, 2011. Spin crossover in ferropericlase at high pressure: a seismologically transparent transition? *Science,* **331,** 64–67.

Babuska, V. & Cara, M., 1991. *Seismic Anisotropy in the Earth. Modern Approaches in Geophysics 10,* Kluwer Academic Publishers.

Bachmann, F., Hielscher, R. & Schaeben, H., 2010. Texture analysis with MTEX – free and open source software toolbox, *Solid State Phenom.,* **160,** 63–68.

Blackman, D.K., Kendall, J.M., Dawson, P.R., Wenk, H.-R., Boyce, D. & Morgan, J.P., 1996. Teleseismic imaging of subaxial flow at mid-ocean ridges: travel-time effects of anisotropic mineral texture in the mantle, *Geoph. J. Int.,* **127,** 415–426.

Blackman, D.K., Wenk, H.-R. & Kendall, J.M., 2002. Seismic anisotropy of the upper mantle 1. Factors that affect mineral texture and effective elastic properties, *Geochem., Geophys., Geosyst.,* **3,** 1–24.

Boioli, F., Carrez, P., Cordier, P., Devincre, B., Gouriet, K., Hirel, P., Kraych, A. & Ritterbex, S., 2017. Pure climb creep mechanism drives flow in Earth's lower mantle, *Sci. Adv.,* **3,** e1601958, doi:10.1126/sciadv.1601958.

Browaeys, J.T. & Chevrot, S., 2004. Decomposition of the elastic tensor and geophysical applications, *Geophys. J. Int.,* **159**(2), 667–678.

Bullen, K.E., 1949. Compressibility-pressure hypothesis and the Earth's interior, *Geophys. J. Int.,* **5,** 335–368.

Chandler, B., Bernier, J., Diamond, M., Kunz, M. & Wenk, H.-R., 2021. Exploring microstructures in lower mantle mineral assemblages with synchrotron x-rays, *Sci. Adv.,* **7,** eabd3614, doi:10.1126/sciadv.abd3614.

Cottaar, S., Li, M., McNamara, A.K., Romanowicz, B. & Wenk, H.-R., 2014. Synthetic seismic anisotropy models within a slab impinging on the core–mantle boundary, *Geophys. J. Int.,* **199,** 164–177.

Cottaar, S. & Romanowicz, B., 2013. Observations of changing anisotropy across the southern margin of the African LLSVP, *Geophys. J. Int.,* **195,** 1184–1195.

Dawson, P. & Wenk, H.R., 2000. Texturing of the upper mantle during convection, *Phil. Mag. A,* **80**(3), 573–598.

Dobson, D.P., Lindsay-Scott, A., Hunt, S.A., Bailey, E., Wood, I.G., Brodholt, J.P., Vocadlo, L. & Wheeler, J., 2013. Strong inheritance of texture between perovskite and post-perovskite in the D′′ layer, *Nat. Geosci.,* **6,** 575–578.

Dobson, D.P., Lindsay-Scott, A., Hunt, S.A., Bailey, E., Wood, I.G., Brodholt, J.P., Vocadlo, L. & Wheeler, J., 2019. Anisotropic diffusion creep in postperovskite provides a new model for deformation at the core−mantle boundary, *PNAS,* **116,** 26389–26393.

Dziewonski, A.M. & Anderson, D.L., 1981. Preliminary reference Earth model, *Phys. Earth planet. Inter.,* **25,** 297–356.

Eshelby, J., 1957. The determination of the elastic field of an ellipsoidal inclusion, and related problems, *Proc. R. Soc. Lond.,* **241,** 376–396.

Ford, H.A. & Long, M.D., 2015. A regional test of global models for flow, rheology, and seismic anisotropy at the base of the mantle, *Phys. Earth Planet. Inter.,* **245,** 71–75.

Garnero, E.J., Maupin, V., Lay, T. & Fouch, M.J., 2004. Variable azimuthal anisotropy in Earth's lowermost mantle, *Science,* **306,** 259–261.

Gleeson, M.L.M. & Gibson, S.A., 2019. Crustal controls on apparent mantle pyroxenite signals in ocean-island basalts, *Geology,* **47,** 321–324.

Gleeson, M.L.M., Gibson, S.A. & Williams, H.M., 2020. Novel insights from Fe-isotopes into the lithological heterogeneity of Ocean Island Basalts and plume-influenced MORBs, *Earth Planet. Sci. Lett.,* **535,** 116114.

Goryaeva, A.M., Carrez, P. & Cordier, P., 2016. Low viscosity and high attenuation in $MgSiO_3$ post-perovskite inferred from atomic-scale calculations, *Sci. Rep.,* **6,** 1–10.

Goryaeva, A.M., Carrez, P. & Cordier, P., 2017. Modeling defects and plasticity in $MgSiO_3$ post-perovskite: part 3—Screw and edge [001]dislocations, *Phys. Chem. Miner.,* **44,** 521–533.

Hager, B.H. 1984. Subducted slabs and the geoid: constraints on mantle rheology and flow, *J. geophys. Res.,* **89**(B7), 6003–6015

Hernlund, J.W., Thomas, C. & Tackley, P.J., 2005. A doubling of the post-perovskite phase boundary and structure of the Earth's lowermost mantle, *Nature,* **434,** 882–886.

Hirose, K., Sinmyo, R., Sata, N. & Ohishi, Y., 2006. Determination of post-perovskite phase transition boundary in $MgSiO_3$ using Au and MgO pressure standards, *Geophys. Res. Lett.,* **33**(1), doi:10.1029/2005GL024468.

Karato, S., 2010. The influence of anisotropic diffusion on the high-temperature creep of a polycrystalline aggregate, *Phys. Earth Planet. Inter.,* **183,** 468–472.

Karato, S., 2011. Rheological structure of the mantle of a super-Earth: some insights from mineral physics, *Icarus,* **212,** 14–23.

Karki, B.B., Wentzcovitch, R.M., de Gironcoli, S. & Baroni, S., 2000. High-pressure lattice dynamics and thermoelasticity of MgO, *Phys. Rev. B,* **61,** 8793–8800.

Kasemer, M., Zepeda-Alarcon, E., Carson, R., Dawson, P. & Wenk, H.-R., 2020. Deformation heterogeneity and intragrain lattice misorientations in high strength contrast dual-phase bridgmanite/periclase, *Acta Mater.,* **189,** 284–298.

Kawai, K. & Tsuchiya, T., 2009. Temperature profile in the lowermost mantle from seismological and mineral physics joint modeling, *Proc. Natl. Acad. Sci.,* **106,** 22119–22123.

Kawai, K. & Tsuchiya, T., 2015. Small shear modulus of cubic $CaSiO_3$ perovskite, *Geophys. Res. Lett.,* **42,** 2718–2726.

Kocks, U.F., Tomé, C.N. & Wenk, H.-R., 2000. *Texture and Anisotropy: Preferred Orientations in Polycrystals and Their Effect on Materials Properties,* Cambridge Univ. Press.

Lebensohn, R.A. & Tomé, C.N., 1993. A self-consistent anisotropic approach for the simulation of plastic deformation and texture development of polycrystals: application to zirconium alloys, *Acta Metall. Mater.,* **41,** 2611–2624.

Lebensohn, R.A., Tomé, C.N. & CastaÑeda, P.P., 2007. Self-consistent modelling of the mechanical behaviour of viscoplastic polycrystals incorporating intragranular field fluctuations, *Philos. Mag.,* **87**(28), 4287–4322.

Li, M. & Zhong, S., 2017. The source location of mantle plumes from 3D spherical models of mantle convection, *Earth Planet. Sci. Lett.,* **478,** 47–57.

Li, Y., Deschamps, F. & Tackley, P.J., 2014. Effects of low-viscosity post-perovskite on the stability and structure of primordial reservoirs in the lower mantle, *Geophys. Res. Lett.,* **41,** 7089–7097.

Lin, F., Couper, S., Jugle, M. & Miyagi, L., 2019. Competing deformation mechanisms in periclase: implications for lower mantle anisotropy, *Minerals,* **9**(11), 650.

Long, M.D., 2009. Complex anisotropy in D″ beneath the eastern Pacific from SKS–SKKS splitting discrepancies, *Earth Planet. Sci. Lett.,* **283,** 181–189.

Lynner, C. & Long, M.D., 2014. Lowermost mantle anisotropy and deformation along the boundary of the African LLSVP, *Geophys. Res. Lett.,* **41,** 3447–3454.

Mainprice, D., Tommasi, A., Ferré, D., Carrez, P. & Cordier, P., 2008. Predicted glide systems and crystal preferred orientations of polycrystalline silicate Mg-perovskite at high pressure: implications for the seismic anisotropy in the lower mantle, *Earth Planet. Sci. Lett.,* **271**(1), 135–144.

Marquardt, H. & Miyagi, L., 2015. Slab stagnation in the shallow lower mantle linked to an increase in mantle viscosity, *Nat. Geosci.,* **8,** 311–314.

Marquardt, H., Speziale, S., Reichmann, H.J., Frost, D.J., Schilling, F.R. & Garnero, E.J., 2009. Elastic shear anisotropy of ferropericlase in Earth's lower mantle, *Science,* **324,** 224–226.

McNamara, A.K., van Keken, P.E. & Karato, S.-I., 2002. Development of anisotropic structure in the Earth's lower mantle by solid-state convection, *Nature,* **416,** 310–314.

McNamara, A.K., van Keken, P.E. & Karato, S.I., 2003. Development of finite strain in the convecting lower mantle and its implications for seismic anisotropy, *J. geophys. Res.,* **108,** 2230, B5.

Merkel, S. *et al.*, 2007. Deformation of (Mg,Fe)SiO3 post-perovskite and D" anisotropy, *Science,* **316,** 1729–1732.

Miyagi, L., Kanitpanyacharoen, W., Kaercher, P., Lee, K.K.M. & Wenk, H.-R., 2010. Slip Systems in $MgSiO_3$ Post-perovskite: implications for D″ anisotropy, *Science,* **329,** 1639–1641.

Miyagi, L., Kanitpanyacharoen, W., Stackhouse, S., Militzer, B. & Wenk, H.-R., 2011. The enigma of post-perovskite anisotropy: deformation versus transformation textures, *Phys Chem Miner.,* **38,** 665–678.

Miyagi, L., Merkel, S., Yagi, T., Sata, N., Ohishi, Y. & Wenk, H.-R., 2009. Diamond anvil cell deformation of $CaSiO_3$ perovskite up to 49GPa, *Phys. Earth Planet. Inter.,* **174**(1), 159–164.

Miyagi, L. & Wenk, H.-R., 2016. Texture development and slip systems in bridgmanite and bridgmanite + ferropericlase aggregates, *Phys. Chem. Min.,* **43**(8), 597–613.

Muir, J. & Brodholt, J., 2018. Water distribution in the lower mantle: implications for hydrolytic weakening, *Earth Planet. Sci. Lett.,* **484,** 363–369.

Nakagawa, T. & Tackley, P.J., 2011. Effects of low-viscosity post-perovskite on thermo-chemical mantle convection in a 3-D spherical shell, *Geophys. Res. Lett.,* **38,** L04309, doi:10.1029/2010GL046494.

Nomura, R., Hirose, K., Uesugi, K., Ohishi, Y., Tsuchiyama, A., Miyake, A. & Ueno, Y., 2014. Low core-mantle boundary temperature inferred from the solidus of pyrolite, *Science,* **343,** 522–525.

Nowacki, A., Wookey, J. & Kendall, J.-M., 2010. Deformation of the lowermost mantle from seismic anisotropy, *Nature,* **467,** 1091–1094.

Nowacki, A., Wookey, J. & Kendall, J.-M., 2011. New advances in using seismic anisotropy, mineral physics and geodynamics to understand deformation in the lowermost mantle, *J. Geodyn.,* **52,** 205–228.

Oganov, A.R. & Ono, S., 2004. Theoretical and experimental evidence for a post-perovskite phase of $MgSiO_3$ in Earth's D″ layer, *Nature,* **430,** 445–448.

Panning, M. & Romanowicz, B., 2006. A three-dimensional radially anisotropic model of shear velocity in the whole mantle, *Geophys. J. Int.,* **167,** 361–379.

Pisconti, A., Thomas, C. & Wookey, J., 2019. Discriminating between causes of D″ anisotropy using reflections and splitting measurements for a single path, *J. geophys. Res.,* **124,** 4811–4830.

Romanowicz, B. & Wenk, H.-R., 2017. Anisotropy in the deep Earth, *Phys. Earth Planet. Inter.,* **269,** 58–90.

Simmons, N.A. & Grand, S.P., 2002. Partial melting in the deepest mantle, *Geophys. Res. Lett.,* **29,** 47–1-47-4.

Sturgeon, W., Ferreira, A.M.G., Faccenda, M., Chang, S.-J. & Schardong, L., 2019. On the origin of radial anisotropy near subducted slabs in the midmantle, *Geochem. Geophys.,* **20,** 5105–5125.

Tackley, P.J., 2011. Living dead slabs in 3-D: the dynamics of compositionally-stratified slabs entering a "slab graveyard" above the core-mantle boundary, *Phys. Earth Planet Inter.,* **188,** 150–162.

Tommasi, A., Goryaeva, A., Carrez, P., Cordier, P. & Mainprice, D., 2018. Deformation, crystal preferred orientations, and seismic anisotropy in the Earth's D″ layer, *Earth Planet. Sci. Lett.,* **492,** 35–46.

Tsuchiya, T., Tsuchiya, J., Umemoto, K. & Wentzcovitch, R.M., 2004. Elasticity of post-perovskite $MgSiO_3$, *Geophys. Res. Lett.,* **31**(14), L14603, doi:10.1029/2004GL020278.

Walker, A.M., Dobson, D.P., Wookey, J., Nowacki, A. & Forte, A.M., 2018. The anisotropic signal of topotaxy during phase transitions in D″, *Phys. Earth Planet. Inter.,* **276,** 159–171.

Walker, A.M., Forte, A.M., Wookey, J., Nowacki, A. & Kendall, J.-M., 2011. Elastic anisotropy of D″ predicted from global models of mantle flow: predicting anisotropy in D″, *Geochem. Geophys. Geosyst.,* **12,** 10.

Walker, A.M. & Wookey, J., 2012. MSAT—A new toolkit for the analysis of elastic and seismic anisotropy, *Comput. Geosci.,* **49,** 81–90.

Wenk, H.-R., Canova, G., Brechet, Y. & Flandin, L., 1997. A deformation-based model for recrystallization of anisotropic materials, *Acta Mater.,* **45,** 3283–3296.

Wenk, H.-R., Cottaar, S., Tomé, C.N., McNamara, A. & Romanowicz, B., 2011. Deformation in the lowermost mantle: from polycrystal plasticity to seismic anisotropy, *Earth Planet. Sci. Lett.,* **306,** 33–45.

Wenk, H.-R., Speziale, S., McNamara, A.K. & Garnero, E.J., 2006. Modeling lower mantle anisotropy development in a subducting slab, *Earth Planet. Sci. Lett.,* **245**(1), 302–314.

Wenk, H.-R. & Tomé, C.N., 1999. Modeling dynamic recrystallization of olivine aggregates deformed in simple shear, *J. geophys. Res.,* **104**(B11), 25 513–25 527.

Wheeler, J., 2009. The preservation of seismic anisotropy in the Earth's mantle during diffusion creep, *Geophys. J. Int.,* **178,** 1723–1732.

Williams, Q. & Garnero, E.J., 1996. Seismic evidence for partial melt at the base of Earth's mantle, *Science,* **273,** 1528–1530.

Wu, X., Lin, J.-F., Kaercher, P., Mao, Z., Liu, J., Wenk, H.-R. & Prakapenka, V.B., 2017. Seismic anisotropy of the D″ layer induced by (001) deformation of post-perovskite, *Nat. Commun.,* **8,** 14669.

Wu, Z., 2016. Velocity structure and composition of the lower mantle with spin crossover in ferropericlase, *J. geophys. Res.,* **121**(4), 2304–2314.

Yang, J., Tong, X., Lin, J.-F., Okuchi, T. & Tomioka, N., 2015. Elasticity of ferropericlase across the spin crossover in the Earth's lower mantle, *Sci. Rep.,* **5**(1), 17188.

Yuan, K. & Romanowicz, B., 2017. Seismic evidence for partial melting at the root of major hot spot plumes, *Science,* **357,** 393–397.

Yue, B., Hong, F., Hirao, N., Vasin, R., Wenk, H.-R., Chen, B. & Mao, H.-K., 2019. A simple variant selection in stress-driven martensitic transformation, *PNAS,* **116,** 14905–14909

Zhang, L. *et al.*, 2014. Disproportionation of (Mg,Fe)SiO3 perovskite in Earth's deep lower mantle, *Science,* **344,** 877–882.

Zhang, S., Cottaar, S., Liu, T., Stackhouse, S. & Militzer, B., 2016. High-pressure, temperature elasticity of Fe- and Al-bearing $MgSiO_3$: implications for the Earth's lower mantle, *Earth Planet. Sci. Lett.,* **434,** 264–273.

Zhong, S., 2006. Zhong, S., 2006. Constraints on thermochemical convection of the mantle from plume heat flux, plume excess temperature, and upper mantle temperature, *J. geophys. Res. Solid Earth,* **111**(B4), doi:10.1029/2005JB003972